Sabin Kumar Karki

Beam-steerable E-band lens antenna for 5G backhaul link

School of Electrical Engineering

Thesis submitted for examination for the degree of Master of Science in Technology.

Espoo 10.10.2016

Thesis supervisor:

Prof. Ville Viikari

Thesis instructor:

Dr. Juha Ala-Laurinaho

Aalto University
School of Electrical
Engineering

AALTO UNIVERSITY
SCHOOL OF ELECTRICAL ENGINEERING

ABSTRACT OF THE
MASTER'S THESIS

Author: Sabin Kumar Karki

Title: Beam-steerable E-band lens antenna for 5G backhaul link

Date: 10.10.2016 Language: English Number of pages:12+70

Department of Radio Science and Engineering

Professorship: Radio Science Code: S-26

Supervisor: Prof. Ville Viikari

Instructor: Dr. Juha Ala-Laurinaho

5G high throughput requirement can only be met with dense network architecture and wide channel bandwidth available in E-band i.e. (71-76)GHz/(81-86)GHz spectrum. Millimeter wave propagation loss and high capacity requirement appeal for directional antenna with beam steering capability. A feasibility study of antenna types is conducted for the 5G millimeter wave backhaul link application.

The main objective of this thesis is first to conduct feasibility study and then to design, fabricate and measure an integrated lens antenna (ILA) fulfilling the regulations for point-to-point link antennas in E-band. Various ILA performance optimization methods and their applicability are studied. In-house ray tracing program is used to study characteristics of the ILA and to design an antenna demonstrating desired performance. Optimization results showed that the materials with the dielectric constant ϵ_r in range of 3 - 5 gives the maximum gain performance. Based on dielectric properties and commercial availability, the HDPE material is found to be most suitable. Free space dielectric properties measurement confirmed dielectric constant of HDPE ϵ_r as 2.31.

Two elliptical ILAs were designed to meet given regulations at boresight and up to 5° beam steering angle respectively. Proposed First Lens with 160 mm diameter achieved the 38 dBi gain criteria at boresight direction at 73.5 GHz. Measurement of the fabricated prototype lens showed 1.48° HPBW, $-$ 17.6 dB side lobe level and scan loss for 5° was found to be 2.05 dB. Congruence between the simulation and measurement results highlights the validity of the in-house simulation tool. According to the simulation results, Second Lens designed with 210 mm diameter and 0.95 eccentricity factor meets the given regulation upto 5° beam steering angle with 0.9 dB scan loss.

Keywords: 5G, backhaul, dielectric properties measurement, integrated lens antenna, millimeter wave, planar near-field measurement, ray tracing

Acknowledgments

This thesis is the outcome of my work done at the Department of Radio Science and Engineering, Aalto University School of Electrical Engineering. The thesis is also part of E-band lens antenna for backhaul radio link (Elens) project carried out by Aalto University in cooperation with Nokia and VTT. The objective is to design an Integrated Lens Antenna (ILA) capable of 2D beam steering and fulfilling current regulations for the back-haul link antennas. Writing this thesis has been a wonderful learning experience and has a big impact on me.

I would like to thank Professor Ville Viikari for providing me this opportunity and agreeing to supervise my thesis. I would like to express my sincere gratitude to my advisor Dr. Juha Ala−Laurinaho for his invaluable guidance, feedback and encouragement throughout the project and thesis writing process. I would also like to thank Mr. Pekka Wainio and Dr. Risto Valkonen from Nokia Bell Labs and everyone involved in ELens project for providing feedback during the project and thesis writing. I am grateful to Dr. Aki Karttunen for MATLAB program and his suggestions and Dr. Jussi Säily for his feed antenna design.

Finally, I would like to thank my family for providing me with unfailing support and continuous encouragement throughout my years of study and writing this thesis, even though they live thousands of kilometers away. To my friends scattered around the world, thank you all for providing much needed distractions at appropriate times.

Sabin Kumar Karki

Otaniemi, 10.10.2016

Contents

Abbreviations and Acronyms

5G	Fifth Generation
CMOS	Complementary Metal−Oxide−Semiconductor
DL	Double Lens
DSL	Double Shell Lens
ETSI	European Telecommunication Standards Institute
FDTD	Finite − Difference Time Domain
FEM	Finite Element Method
FZPL	Fresnel Zone Plate Lens
GaAs	Gallium Arsenide
HDPE	High Density Polyethylene
HPBW	Half Power Beam Width
ILA	Integrated Lens Antenna
IOT	Internet of Things
LOS	Line of Sight
MEMS	Micro Electro Mechanical Systems
MOM	Method Of Moment
MUT	Material Under Test
RPE	Radiation Pattern Envelope
VNA	Vector Network Analyser
XPD	Cross polarization Discrimination

Symbols

a	ellipse semi-major axis [m]
A_A	ray tube cross section area [m ^{2}]
b	ellipse semi-minor axis [m]
c_0	free space speed of light [m/s]
d	array element separation distance [m]
D_{max}	Directivity
e	ellipse eccentricity
$\overline{E}$	electric field strength [V/m]
$\overline{E}_i$	electric field strength incident on dielectric surface [V/m]
$\overline{E}_r$	electric field strength reflected from dielectric surface [V/m]
$\overline{E}_t$	electric field strength refracted from dielectric surface [V/m]
$\overline{E}_i^{\parallel}$	incident electric field parallel polarisation vector [V/m]
$\overline{E}_i^{\perp}$	incident electric field perpendicular polarisation vector [V/m]
$\overline{E}_r^{\parallel}$	reflected electric field parallel polarisation vector [V/m]
$\overline{E}_r^{\perp}$	reflected electric field perpendicular polarisation vector [V/m]
$\overline{E}_t^{\parallel}$	refracted electric field parallel polarisation vector [V/m]
$\overline{E}_t^{\perp}$	refracted electric field perpendicular polarisation vector [V/m]
f	frequency [Hz]
F	focal distance [m]
i	imaginary unit
k	wavenumber [1/m]
k_0	free space wave number [1/m]
K	number of zones
l	ray length [m]
L	extension length [m]
L_{dielec}	dielectric loss
L_{refl}	reflectrion loss in collimating surface [dB]
L_{spill}	spillover loss in extension [dB]
n	refractive index
N	number of rays
P	number of phase correction steps in FZPL
r_n	groove radius of FZPL [m]
R	radius [m]
$\tan\delta$	loss tangent
t	zoning thickness [m]
α	attenuation coefficient [1/m]

β	feeding phase difference between array elements [^{0}]
$\Gamma^{\parallel}$	parallel polarization reflection coefficient
$\Gamma^{\perp}$	perpendicular polarization reflection coefficient
ϵ_r	relative permittivity [As/Vm]
ϵ_0	free space permittivity [As/Vm]
$\epsilon^{"}$	loss factor [As/Vm]
$\epsilon^{'}$	dielectric constant [As/Vm]
η	total antenna efficiency
θ_i	incident angle
θ_r	reflection angle
θ_t	refraction angle
λ	wavelength [m]
λ_0	free space wavelength [m]
$\tau^{\parallel}$	parallel polarization transmission coefficient
$\tau^{\perp}$	perpendicular polarization transmission coefficient
ϕ	array inter-element phase difference [^{0}]

List of Figures and Tables

List of Figures

List of Tables

1 Introduction

1.1 Background

Evolution of mobile communication has always focused on increasing data rates, providing ubiquitous services and accommodating more subscribers. With advent of smartphones, tablets, etc. and the rise of high definition video streaming, cloud computing, remote monitoring, etc. wireless data traffic has increased exponentially. Data traffic handled by the wireless network is expected to multiply 100 times; 3 exabyte traffic in 2010 is forecasted to exceed 500 exabyte by 2020 [1].

5G is the next phase of the mobile telecommunications system. It is expected to have key features like high throughput, low end-to-end latency, incorporation of Internet of Things (IoT), reliability, robustness and provision of ubiquitous service. 5G is expected to have 1-10 Gbps connection to endpoints [2] [3]. Various studies [4] [1] [5] show that such improvement is possible with dense network architecture, an increase in spectral efficiency, and larger bandwidth allocation. High throughput requirement together with complex and dense network structure demands high capacity flexible backhaul link solution. Backhaul link is the transport infrastructure from base stations to the core network. Vision of network topology of 5G is shown in Fig.1

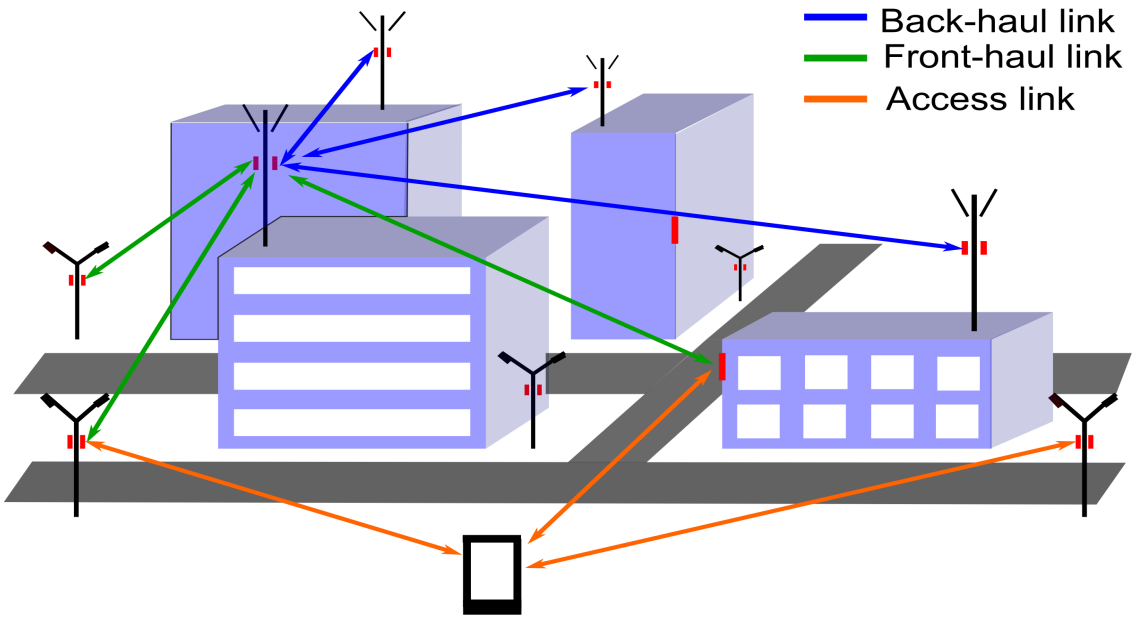

Figure 1: 5G network topology modified from [6]

Fiber access is an obvious choice of technology for high-speed links. In dense small cell network using fiber connection becomes expensive and wiring process becomes complex [7]. Wireless backhaul radio link is proven solution in microwave

range. Wireless backhaul not just supports network densification but also boosts low latency communication between base stations. [7].

Channel information capacity depends on the available bandwidth and the signal to noise ratio (S/N) [8]. Gigabit level throughput can be achieved with larger bandwidth in wireless backhaul link. Technological advances have made millimeter wave devices accessible. Though no specific frequencies have been allocated for 5G at millimeter waves, but 28 GHz, 37-42 GHz, and E-band with 1.3 GHz, 2.1 GHz, and 10 GHz bandwidths respectively are potential candidates [9]. In E-band spectrum i.e. 71-76 GHz and 81-86 GHz, a channel bandwidth of 250 MHz or even 500 MHz is possible [10]. With advanced modulation schemes such as 64 QAM and the channel bandwidth of 250 MHz, peak throughput rate of 2.5 Gbps or even higher is achievable [11].

1.2 Problem Statement

Millimeter wave backhaul links face challenges due to propagation loss and sensitivity to blockage. The free space loss is about 130 dB/km for lower E-band whereas it is 131 dB/km for upper E-band [12]. Rain attenuation at millimeter waves depends on rain rate, for heavy rain i.e. 25 mm/hr attenuation is 10.7 dB/km [13] at E-band frequency. Absorption attenuation due to atmospheric gases at E-band is as low as 0.5 dB/km compared to 15 dB/km at 60 GHz.

Antenna gain, modulation scheme, throughput and hop length are interrelated terms in the modern communications system. Highly efficient modulation schemes are less resilient to system loss. Hop length is directly proportional to propagation loss. Therefore, schemes with high spectral efficiency can be used only with high gain transmitter-receiver antennas. Due to propagation losses and sensitivity to blockage E-band antennas provide shorter hop length and applied in the line of sight (LOS) links compared to microwave link antennas. Millimeter wave system requires 32 dB gain to establish a link with 100 m hop length and an additional 3 dB is required both at transmitter and receiver side to double the hop length distance [14]. European Telecommunication Standards Institute (ETSI) sets minimum gain criteria of 38 dBi for point-to-point fixed radio links for 66-86 GHz frequency range [15]. But high propagation loss also reduces the probability of interference between parallel links at close proximity which helps to improve spatial frequency reuse [9].

To overcome high loss, millimeter wave antennas are required to have high gain above 30 dBi and up to 50 dBi [16]. Generally, microwave link antennas with lower gain are manually aligned at both ends, but millimeter wave antenna have pencil-beam, with 1° - 2° half power beam width (HPBW). Therefore beam steering capability is desired for alignment purpose [16]. Additionally, it would help to find nearby base stations and compensate for sways due to the wind. The capacity of

point-to-point radio link can be doubled by establishing parallel links in orthogonal polarization modes in the same frequency channel [17]. Cross-coupling between these links can be minimized with high cross polarization discrimination (XPD) of dual-polarized link antenna.

1.3 Objective of the Thesis

The main objective of this thesis is to conduct a feasibility study of an Integrated Lens Antenna (ILA) capable of 2D beam steering that fulfils regulation for point-to-point antennas in E-band. Later, detailed design, fabrication, and measurements are conducted. Detailed requirements for the antenna are summarized in Table 1. All requirements must be met for each beam steering angle.

Table 1: Lens antenna specification for the point-to-point link antenna

Frequency range of operation	71-76 GHz
Directivity	40 dB or higher
Gain	38 dBi or higher
Radiation pattern envelope (RPE)	According to ETSI EN 302 217−4−2 class 2 [15].
Cross polarization discrimination	No requirement for the main lobe only for cross polar RPE
Cross polarization RPE	According to ETSI EN 302 217−4−2 class 2
Beam scan range	Minimum ±5° elevation, ±5°azimuth
Beam overlap	−3 dB
Polarization	Single, vertical

Specifically, the lens performance is evaluated against the requirements for gain, radiation pattern envelopes (RPEs), and cross-polar discrimination (XPD). Apart from designing ILA, objective of this thesis is to do a literature review of different types of antennas that are feasible for given requirements and optimization methods for lens antenna that can be helpful to improve ILA performance. Also, a brief study regarding suitable lens material with respect to the lens dimensions and other manufacturing aspects are done.

1.4 Methodology and Related Work

Lens antenna is electrically large structure. Therefore ray tracing simulation is used to verify antenna characteristics instead of full wave electromagnetic simulation methods. In this project, MATLAB based ray tracing program developed by Aki Karttunen, Aalto University is used to verify the lens performance [18]. The designed lens is fabricated and measured to verify simulation results.

In the feasibility study, relations between various lens parameters and lens characteristics is studied and later based on these relation lens is designed that complies

with above requirements. Feasible beam steering range and feed geometry were specified. Finally, the lens is fabricated and characterized.

This thesis is part of E-band lens antenna for backhaul radio link (ELens) project carried out by Aalto University in cooperation with Nokia and VTT.

1.5 Structure of the Thesis

This thesis is divided into eight major chapters which proceed as follows. In Chapter 2, we study feasible antenna types that meet given requirement. Chapter 3 introduces integrated lens antenna, design process, and performance optimization techniques. In Chapter 4 ray tracing is explained. Then in Chapter 5, ray tracing simulation results are presented. Chapter 6 will focus on dielectric properties measurement process and results. Chapter 7 will demonstrate antenna measurement techniques and results. Finally, conclusions are drawn in Chapter 8.

2 Beam Steering Antennas

2.1 Introduction

In this chapter, we will discuss different antenna types that are feasible for millimeter wave backhaul link application. Rather than theoretical detail, we will focus on antenna properties such as gain, loss, beam steering range, bandwidth, size, and cost. Overall performance of various antenna types will be evaluated. Feasibility of various antennas will be estimated.

2.2 Phased Array

Phased array is an array of antenna elements whose excitation phase is controlled in order to get desired beam steering angle. Phases of antenna elements can be controlled with phase shifters or delay circuits. Block diagram of phased array is shown in Figure 3. Phased array is a conventional way of electronic beam steering with high scanning rate compared to mechanical beam steering [19]. Array not just increase main beam directivity, it is also possible to cancels interference from the particular set of direction and estimate the direction of the arrival of incoming signal and improves SINR (Signal to interference plus noise ratio). Interference cancellation in phased array requires extra algorithm which is yet to be implemented.

Directive gain D_{ar} of a phased array with isotropic radiating elements is given by

$$D_{ar} = \frac{2 \cdot k \cdot d \cdot (AF)^2_{max}}{\int_{k \cdot d + \beta}^{-k \cdot d + \beta} |AF(\phi))|^2 \, d\phi} \tag{1}$$

where k is wavenumber, d is separation distance between array elements that varies from $\lambda/2$ to λ to avoid grating lobes. M and N is number of array elements in along x and y axis for planar array. AF is two dimensional array factor that is calculated as

$$AF = \left[\frac{1}{M}\frac{\sin(\frac{M \cdot \phi_x}{2})}{\sin(\frac{\phi_x}{2})}\right] \cdot \left[\frac{1}{N}\frac{\sin(\frac{N \cdot \phi_y}{2})}{\sin(\frac{\phi_y}{2})}\right] \tag{2}$$

where ϕ_x and ϕ_y is phase difference in x direction and y direction of planar array respectively. Phase difference between array element is given by

$$\begin{aligned} \phi_x &= k \cdot d_x \cdot cos(\theta) + \beta_x \\ \phi_y &= k \cdot d_y \cdot cos(\theta) + \beta_y \end{aligned} \tag{3}$$

where β_x and β_y is feeding phase difference in x and y dimensions of planar array. Gain of an antenna is a function of directivity and antenna efficiency (η) as shown in the following equation.

$$G = \eta \cdot D_{ar} \tag{4}$$

The gain of a phased array antenna depends on the number of array elements and element spacing [20]. In [14], simulation results showed that approximately 80 $\times$

80 array elements would be required for two-dimensional beam steering with 38 dB boresight gain. Large number of elements increases feeding network complexity and losses in an array. Additionally, the size of an array becomes large and manufacturing cost also increases. A 256 (16×16) element phased array beamforming prototype is designed at 28 GHz with 6-bit phase shifter to achieve 24 dBi gain [21].

Digital phase shifters in high frequencies suffer from high insertion loss. Commercially available CMOS, GaAs, and MEMS based phase shifters have 6.91 - 17 dB, $\geq$ 7.5 dB and 3.21 - 8.2 dB loss respectively at V-band (40 - 75 GHz) [19]. Operation bandwidth of phased array is limited by beam squint phenomena which is caused by non-idealities of phase shifter [22]. Steered beam direction changes as a function of frequency that results in beam widening and reduction of gain. Finite resolution of phase shifters, noise in circuit and channel uncertainty further degrades array performance [23].

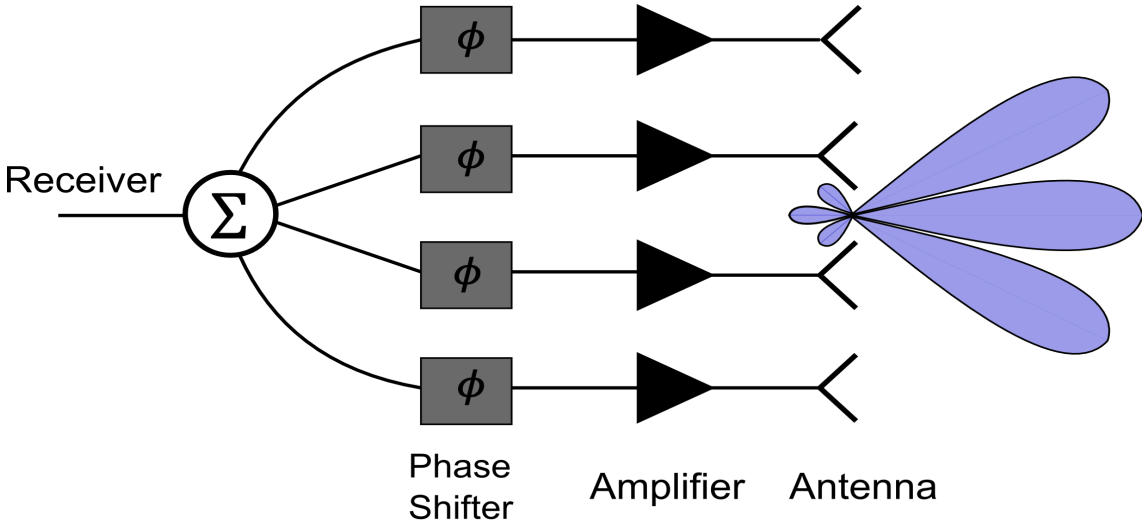

Figure 2: Block diagram of a phased array [24].

2.3 Reflector Antenna

Reflectors antennas are typically known for high gain and they are widely used in point-to-point communication, radio telescopes etc. Large aperture area of reflector surface gives high directive gain [25]. Reflector antenna can be of any arbitrary shape i.e. line, plane, corner, hyperbolic or elliptical but parabolic transforms incoming spherical waves into plane waves [26]. Aperture blockage due to the feed antenna and its supporting structures causes increase in loss, rise in side lobe level and increase in cross-polarization radiation.

Offset reflector antenna not just minimizes aperture blockage effect but also maintains isolation between the feed and the reflector, and also increases (F/D) ratio while maintaining structural rigidity [27]. But in case of linearly polarized feed,

offset reflector antenna reduces polarization purity compared to axis-symmetric reflector, and circular polarized feed beam is squinted from boresight [27].

Spillover, amplitude taper, and phase error are major sources of loss in reflector antenna [20]. Spillover loss is inversely proportional to feed directivity whereas amplitude taper is directly proportional. Therefore, trade-off analysis between spillover and amplitude taper indicates feed with 10 dB edge illumination produces a feasible trafe-off [20]. Non-ideal feed and reflector surface, and frequency dependent nature of feed phase center gives phase error across aperture surface that causes axial defocusing in reflector antenna.

Off-axis feed properties of reflector antenna has been studied for example in [28], [29], [30]. Moving feed position away from axis moves main lobe in direction opposite to feed displacement. Main beam gain reduces and beamwidth increases as increasing feed offset distance. Scan loss depends on focal length to diameter (F/D) ratio and feed position. Smaller F/D results in higher scan loss and vice-versa.

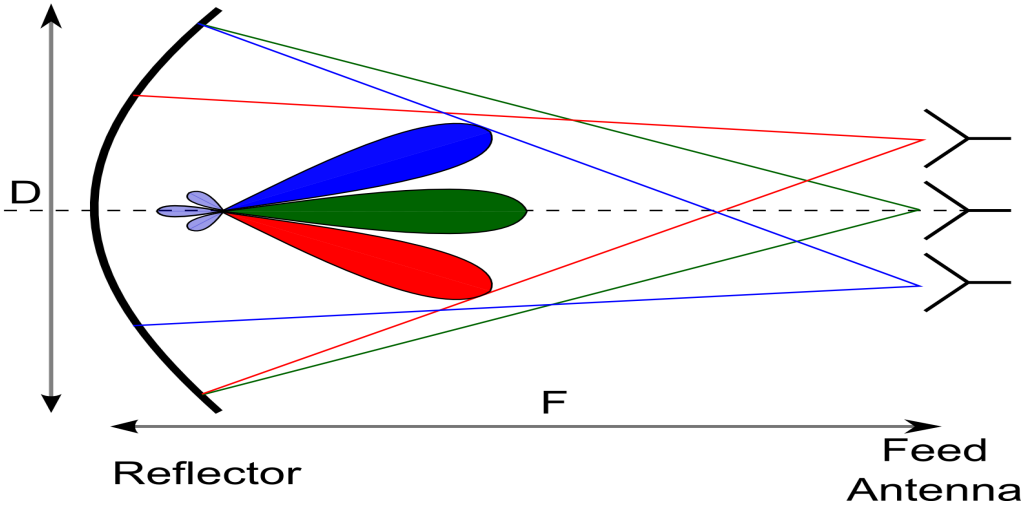

Figure 3: Beam steering with a reflector antenna with a beam switching array feed.

2.4 Reflectarray

Reflectarray is a combination of an array antenna and a reflector. Basically, reflectarray consists of a feed antenna and a reflector surface with an array of reflecting elements. Feed antenna illuminates the reflecting array whose individual element scatters incident field with proper phase required to steer the beam in direction of interest. Re-configurable reflectarray surface can be implemented using patch aperture coupled to varactor loaded line, RF-MEMS loaded lines [31] [32]. Phases of reflecting elements in reflector surface can be defined to form multiple beams towards desired directions, which makes this antenna type suitable solution

for point-to-multipoint communication [33].

Reflectarray has low transmission line loss, but it faces phase error [34]. Reflecting array elements are designed for a fixed frequency and phase error occur if frequency is changed [35]. Phase error minimizes bandwidth of reflectarray. Apart from that refectarray also suffers from dielectric loss, taper loss, and spillover loss [34]. Directivity of reflectarray depends on the total dimension of the reflector surface. Increasing number of reflecting elements would add complexity, size, and manufacturing cost.

A Cassegrain feed reflectarray antenna with 150 mm reflector surface with microstrip patch elements of variabe size gives boresight gain of 36.9 dBi at 77 GHz [34]. In another experiment [36] a folded reflectarray is designed with fixed beams, $\pm$ 60° beam steering range is achieved at 29.5 - 30.8 GHz with 5.5 dB gain scan loss for space application with 116 slot antenna elements spaced at 0.5 λ. A 150 mm reflectarray operating at 120 GHz was designed with conductor backed coplanar patch antenna coupled with MEMS phase shifter [37]. In house genetic algorithm (GA) is used for calculating phase shift pattern to focus at boresight and 9.5° beam steering angle [37].

2.5 Lens Antenna

Lens antenna is a shaped dielectric object used to collimate incident electromagnetic waves from the feed antenna to the desired direction. Operation of lens is based on the refraction (and reflection) of electromagnetic waves at the lens surfaces. Increasing use of higher frequencies, low fabrication cost, easily available dielectric material and modern fabrication technology has fostered use of dielectric lens antenna [38].

Both the reflector antenna and lens antenna work on the same principle of equalization of path length of electromagnetic wave which transforms a spherical wave front to a plane wave. Main advantage of the lens over reflector is that the feed is always behind the lens which nulls aperture blockage by the feed antenna and there is no need of offset solutions [39].

Lens Types

Lens antenna can be categorized based on its shape, feed position and number of refracting surfaces. Based on feed position there are two types, namely:

(i) **Off-body Feed Lens**: Lens with feed antenna at distance of multiple wavelengths from lens body is termed as Off-body feed lens as shown in Figure 4(a).
(ii) **Integrated Feed Lens**: Lenses with feed antenna in direct contact or less than wavelength away from lens body is known as integrated feed lens or integrated lens antenna [38].

Based on number of refracting surfaces lens antenna can be further categorized as:

(i) **Uniform/Homogenous Lens**: Lens made from single dielectric material, which have single refraction surface.
(ii) **Non-Uniform Index Lens**: Lens made from two or more materials with different dielectric properties and have multiple refraction surface is known as non-uniform index lens [38]. As shown in Figure 4(b), Luneburg lens made of layers of various dielectric material is good example of non-uniform index lens.

Based on shape, lens antenna can be categorized as:

(i) **Canonical lens**: Lens with conventional collimating surface such as hemispherical, elliptical, hyperbolical etc. is termed as canonical.
(ii) **Shaped Lens**: Lens with optimized collimating surface to shape radiation pattern in required direction [2]. Double shell lens antenna is an example of shaped lens.

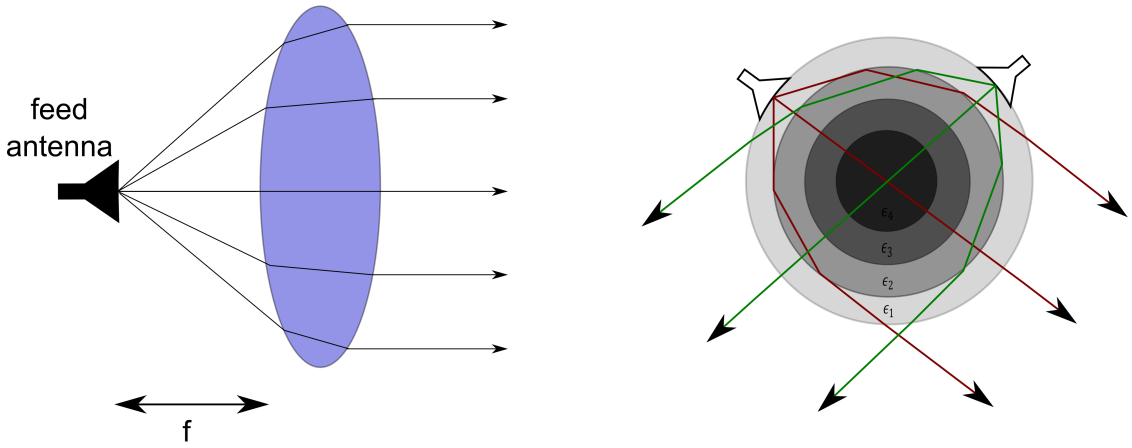

(a) (b)

Figure 4: (a) Off-body feed homogenous focusing lens [39] and (b) an integrated feed Luneburg lens antenna [39].

2.6 Fresnel Zone Plate Lens (FZPL) Antenna

Fresnel Zone Plate Lens (FZPL) antenna is an example of homogenous, shaped lens with off-body feed, as shown in Figure 5. FZPL is planar focusing lens, which has properties similar to lens but works on the principle of interference and diffraction instead of refraction [40]. Like other lens it consists of two elements: primary feed and lens. Fresnel zone plate lens (FZPL) has concentric circular zones of specific radius and location and characteristics. When radiation pass through these zones,

waves diffract and interfere to produce collimated wave on other side. Flat structure of FZPL make it lightweight, small size, and simple for manufacturing. Based on collimating mechanism and shape FZPL can be categorized to two categories: Classical and phase correcting FZPLs, which are described in details in following subsections.

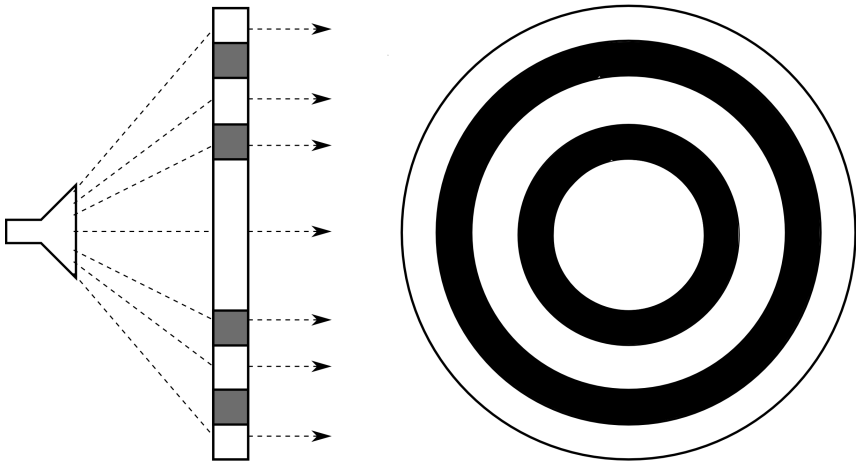

(a) (b)

Figure 5: (a) Fresnel zone plate lens with horn feed and (b) front view of the FZPL.

2.6.1 Classical FZPL

Fresnel zone plate lens consists of alternating transmitting and reflecting zones as shown in Figure 5. Such configuration has less than 15 % aperture efficiency because approximately half of the radiation is reflected from reflecting zones [41]. Other source of loss is diffraction in transmitting zones that does not add perfectly in phase [42].

2.6.2 Phase Correcting FZPL

Phase correcting FZPL lens was first designed at 30 GHz using single dielectric material in 1939 by Bell labs [42]. Phase correction is achieved by annular grooves made in flat dielectric disk as shown in Figure 6. The focusing efficiency of the phase correcting or reversing zone plate is four times higher than that of a classical Fresnel zone plate lens [41]. In order to improve efficiency further, full wave zone is sub-divided into multiple subzones for phase correction in multiple steps. The idea is to do phase correction at discrete intervals so it adds perfectly in phase. Discrete phase correction in sub-zones can be realized with stepped annular grooves as shown in Figure 6(b). Half-wave and quarter wave corrections are used in practice. The

radius of nth annular groove zone is calculated using [43]

$$r_n = \sqrt{nf\lambda + (\frac{n\lambda_0}{P})^2} \tag{5}$$

where λ_0 is free space wavelength, f is focal length and P is number of stages of phase correction, i.e. for half-wave phase correcting FZPL, P equals to 2, and for quarter-wave phase correcting FZPL, P equals to 4.

The groove depth step required for phase reversing is given by

$$\Delta d = \frac{\lambda_0}{P(\sqrt{\epsilon_r} - 1)} \tag{6}$$

$$d = i \cdot \Delta d, i = 0, 1, 2, 3, ...P - 1 \tag{7}$$

where ϵ_r is dielectric constant of lens material. FZPL has narrower bandwidth and its bandwidth is inversely proportional to the number of zones [44]. The efficiency and bandwidth can be improved by varying diameter and thickness of lens [42].

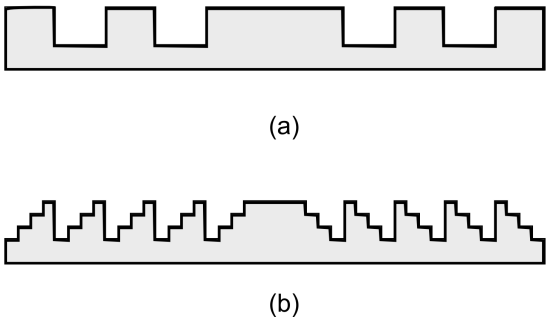

Figure 6: (a) Half wave phase correcting zone plate and (b) a quarter-wave phase correcting zone plate [41].

Planar phase correcting zone plate lens without grooves can also be designed using two or more dielectric materials arranged as concentric rings of equal thickness as shown in Figure 7. Flat structure significantly reduces shadow blockage effect as compared to grooved structure, whereas focusing property remains the same [42]. Permittivity of material is calculated from desired phase shift at any location. Finding real material with calculated permittivity can be challenging for multiple step phase correction FZPL.

2.6.3 Loss in FZPL

Shadow blockage, reflection due to permittivity mismatch and spillover losses are the major contributors to losses in FZPL.

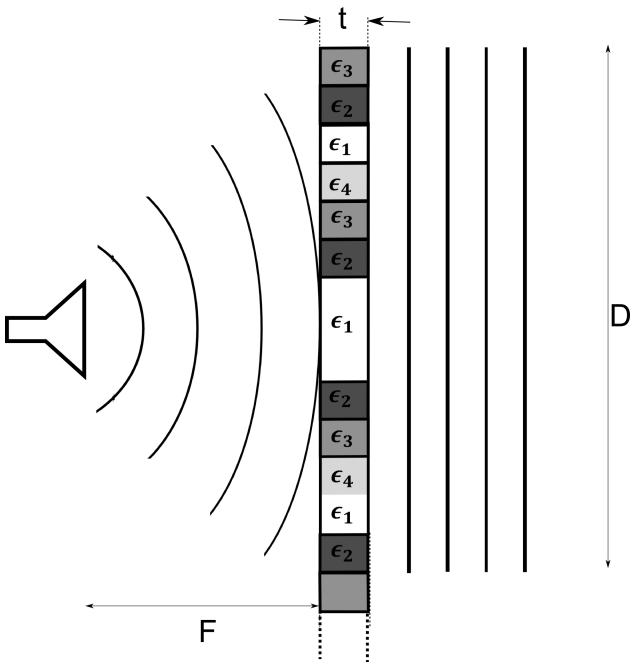

Figure 7: Multi-dielectric phase correcting FZPL.

Shadow Blockage

Rays that hit a groove section perpendicular to the lens axis refracts through lens and add constructively on the other side but the rays that hit the section parallel to the lens axis, i.e. along depth of groove, refracts in a direction that does not add constructively on other side and reduces aperture efficiency. Dark region inside FZPL in Figure 8 shows example of shadow blockage area where rays do not add up constructively on other side.

Shadow efficiency depends on F/D ratio where F is focal length and D is diameter of lens [45]. For electrically large antenna with small F/D ratio, i.e. $D = 14\lambda$ and $F/D = 0.25$, shadow efficiency is 0.4. Shadow efficiency increases to about 0.9 for $F/D = 1$. But, larger F/D ratio would result in increased spillover loss. Modest improvement in shadow efficiency can be achieved from appropriately facing lens i.e. either grooves facing towards the feed antenna or grooves facing away from the feed antenna.

When the focal point of FZPL antenna is brought closer, phase difference across the aperture starts to increase [42]. For FZPL to compensate for phase difference without increasing lens thickness, more zones are required. However, higher number of zones would decrease lens bandwidth.

Mismatch Loss

Mismatch loss is reflection loss caused by permittivity mismatch at air-dielectric interface that decreases aperture efficiency. The amount of reflection depends on

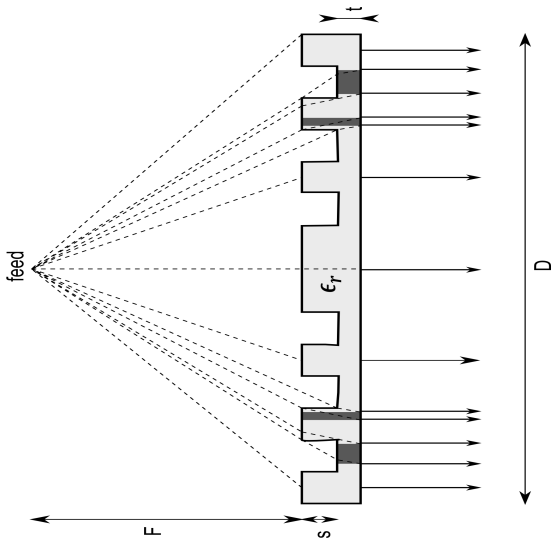

Figure 8: The depiction of shadow blockage in FZPL.

the lens material permittivity, lens thickness and angle of incidence of incoming radiation [42]. As can b e seen from (6) and (7), depth of groove is inversely proportional to dielectric constant of material. Lens with smaller dielectric constant have deeper grooves and that results in lower shadow efficiency. Higher permittivity material have small groove depth but the reflection loss is quite high at the lens-air interface [42]. Therefore, material selection and groove structure should be carefully optimized. Mismatch loss significantly varies with lens thickness (t), therefore, optimized lens thickness helps to improve aperture efficiency [44].

2.6.4 Beam Steering with FZPL

After literature survey on this topic, three methods were found: photo-injected FZPL [46], mechanically reconfigurable FZPL [47], and beamsteering with beam switching feed array [48]. First two solutions are not applicable in our purpose due to slow scanning rate. Beam steering in FZPL can be achieved with offset feed switching array. As feed moves away from focal point in focal plane, main lobe steers from focal axis in opposite direction. Millimeter-wave offset feeding properties of classical FZPL (i.e. with transmitting and reflecting zones) with elliptical zones was studied and beam scanning capability of 15° was achieved [48]. In [49], beam steering with half wave phase correcting FZPL was demonstrated with simulation result. Multi-dielectric (i.e $\epsilon_{r1} = 1.4$ and $\epsilon_{r2} = 2.48$) phase correcting FZPL of 150 mm diameter and 132 mm focal distance with three full wave zones at 60 GHz was manufactured with foam gradient index technology. FZPL had 34.5 dBi directivity and 33.3 dBi gain. Surface efficiency of lens was 31% which could further be improved with higher phase correcting zones. Beam steering range of ± 20°was achieved with 4.1 dB directivity scan loss.

2.7 Integrated Lens Antenna

An integrated lens antenna is canonical lens with a planar integrated feed antenna. Its focusing property, beam steering ability with off-axis feed and small size makes it suitable option for millimeter wave backhaul link antenna. An ILA with 260 mm diameter is designed for 71-76/81-86 GHz frequency bands. Boresight gain of 36.6 dB and beam steering range of $\pm$ 1.5° with maximum 1.9 dB scan loss was achieved with aperture coupled feed antenna [50]. In [51], 95 mm diameter integrated lens antenna with $\pm$ 16.2° beam steering capability was designed with boresight gain of 31.7 dB and scan loss of 3.2 dB.
Detail about integrated lens antenna will be studied in coming chapter.

2.8 Summary

Five different antenna types: phased array, reflector antenna, reflectarray, Fresnel zone plate lens, and integrated lens were studied and found to be feasible for millimeter wave beam steering antenna. In this thesis we will consider elliptical integrated lens antenna for backhaul link. Details of ILA would be studied in following chapter.

3 Integrated Lens Antenna (ILA)

3.1 Introduction

An Integrated lens antenna (ILA) is a combination of a lens body and feed antenna positioned at direct contact of the lens body which eliminates substrate modes and increases the radiation efficiency [39]. Such a configuration also increases mechanical and thermal stability. The ILA can be of any canonical shape (e.g. elliptical, hemispherical, hyperbolical, etc.) depending on requirements [52]. For a small beam steering angle, an elliptical lens gives better performance whereas a hemispherical lens is suitable for large beam steering angles [53]. ILA bends rays radiated by the feed antenna towards the broadside direction, which sharpens the field pattern and increases the directivity and gain. The elliptical ILA also obeys Abbe sine condition, which ensures that all the rays are focused at a point [38].

From Figure 9, we can see that the ILA is divided into two parts: a collimating part and ans extension part. Only rays hitting collimating part are focused therefore absorbers are used along the extension length, as shown in Figure 9, to prevent the radiation exiting from the extension, which helps to reduce the side-lobe levels.

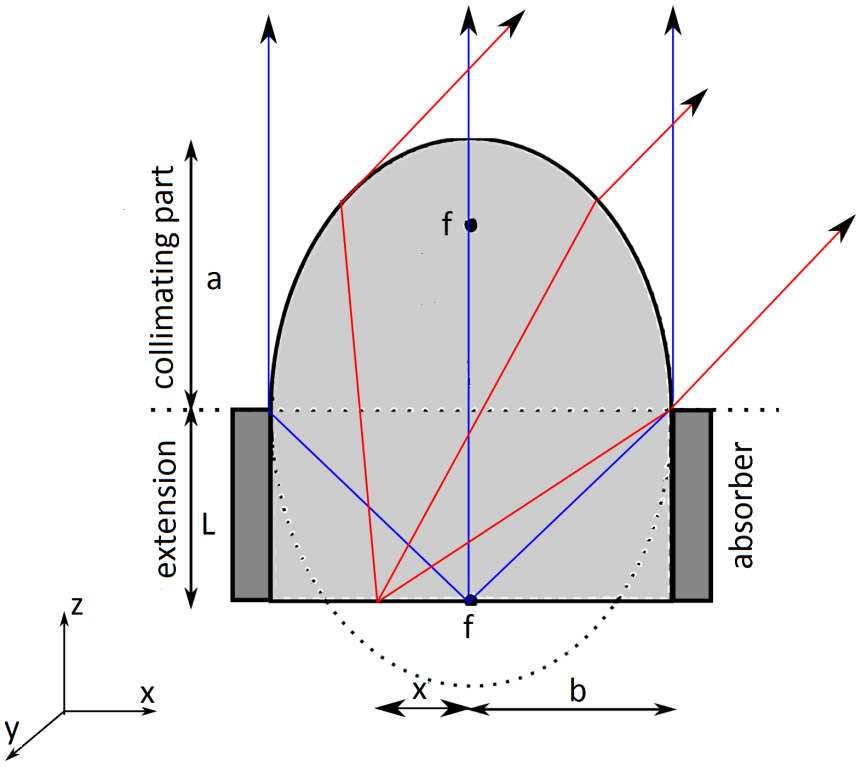

Figure 9: Schematics of the integrated lens antenna (ILA).

3.2 ILA Design

ILA with elliptical collimating surface is designed using equation of ellipse

$$\left(\frac{x}{a}\right)^2 + \left(\frac{y}{b}\right)^2 = 1 \tag{8}$$

where a is the major axis of ellipse, b is the minor axis of ellipse. ILA is a three-dimensional structure formed by solid of revolution of ellipse formed by equation (8) around z-axis. Length of extension is given by

$$L = e \cdot a \tag{9}$$

where e is eccentricity of ellipse. For given relative permittivity (ϵ_r) of material, eccentricity of lens is calculated by

$$e = \frac{1}{\sqrt{\epsilon_r}} = \sqrt{1 - \left(\frac{b}{a}\right)^2}. \tag{10}$$

Absorbers are used along extension length so that rays coming from extension does not affect far-field radiation pattern.

3.3 Beam steering with ILA

Beam steering is achieved in dielectric lens antenna by moving feed source away from the focal point along the focal plane [54]. As the feed moves away from the axis, the beam starts to tilt away from the focal axis. In mechanical beam steering process, lens itself can be moved or tilted keeping source fixed [54]. In the reference, $\pm$ 45 $^\circ$ beam steering was achieved by tilting lens up-to $\pm$ 50 $^\circ$ with 20 mm diameter polyethylene lens at 60 GHz. Scan loss over entire beamsteering angle was less than 1.1 dB.

The direction of the steered beam θ_{steer} can be calculated as

$$\sin(\theta_f) = \frac{\sin(\theta_{\text{steer}})}{\sqrt{\epsilon_r}} \tag{11}$$

where θ_f is angle of incidence at lens surface with respect to lens axis. Beam steering property of a ILA depends on feed offset position, height of lens, and dielectric constant of material used [55]. Phase aberration is introduced by feed displacement in x-direction which reduces the lens directivity. Reduction in the lens directivity is caused by degradation in focusing ability at offset positions, displacement of feeds from focal arc and reduction in projected area of the lens. Such effect can be minimized by applying feed displacement in z-direction. Therefore, moving feed along focal arch would give better directivity at higher offset positions.

Beam steering can be done with beam switching feed array [56]. Array of feed antennas is placed in focal plane which is controlled by a switching network [51].

At given time only one feed element is radiating and its offset from focal point and lens material determines steering angle. As the feed antenna moves to higher offset position along focal plane, scan loss starts to appear due to defocusing effects. [57].

3.4 Losses in ILA

Losses in ILA can be categorized in three parts: reflection loss, dielectric loss, and spillover loss. In general, loss in lens depends on the permittivity of material, loss tangent, and scan angle.

3.4.1 Reflection Loss

Reflection loss is defined as the part of transmitted energy that is reflected back to the source or to undesired direction. In ILA, reflection occurs at lens-air interface. Reflection loss is caused by mismatch in permittivity between lens material and air. Reflection loss depends on angle of incidence of rays at lens-air boundary. Increase in angle of incidence will increase reflection coefficient and after critical angle rays will be totally reflected. Higher permittivity lens have bigger reflection losses, for example material like silicon (ϵ_r=11.7), without any matching layer has reflection loss of 1.5 dB (i.e. 30% of the total power) for zero angle of incidence [58]. These reflected rays eventually exit the lens to undesired directions, after some dielectric loss, reducing directivity of the lens and increasing side lobe level. Therefore second order ray tracing of reflected wave may become important to trace these reflected rays [58]. For beam steering the feed is displaced from the axis. However with increasing off-axis feed distance, reflection loss increases. Reason for such increase is mostly total internal reflection of more rays. Reflection losses in high permittivity lens material can be minimized by using quarter wave matching layer in lens-air boundary [39]. However, the total reflection area remains almost the same.

3.4.2 Spillover Loss

Rays exiting from the extension are not collimated and it increases side lobe level. Therefore there is no reason to allow these rays to leak to far-field. Thus, all electromagnetic energy going into extension part of ILA is considered as spillover. Absorbers are used along extension length to reduce radiation [51]. Also, shaping of the extension is used to avoid reflections. Feed directivity and length of extension (L) are two factors that directly affect spillover loss.

3.4.3 Dielectric Loss

Dielectric loss in ILA is power loss between feed and lens surface due to material dissipation. It is parameterized in terms of loss tangent (tanδ), which is defined as

$$\tan\delta = \frac{\epsilon''}{\epsilon'} \tag{12}$$

where ϵ' and ϵ'' are real and imaginary part of complex dielectric constant respectively. i.e. $\epsilon = \epsilon' - i \cdot \epsilon''$ Attenuation constant (1/m) due to dielectric loss is expressed as

$$\alpha_d = \frac{\pi \cdot \sqrt{\epsilon_r} \cdot \tan\delta}{\lambda_0} \tag{13}$$

Above equation shows that dielectric loss is directly proportional to loss tangent, frequency and square root of dielectric constant. Properties of dielectric material are sensitive to change of temperature. Dielectric losses increase with increase in temperature [59].

3.4.4 Scan Loss

The decrease in gain of beam-steering antenna with increase in scan angle is termed as scan loss [60]. Reduction in gain is a combined effect of decrease in directivity and increase in losses (i.e. reflection loss and spillover loss) [61]. Decrease in directivity is contributed by reduction of projected area, displacement of feed from focal arc and inclined illumination of rays in collimation surface. Effect of projected area reduction can be approximated as cosine reduction of effective aperture area for scanned directions [61]. Directivity reduction can be approximated as

$$D(\theta) = D(0) \cdot \cos(\theta) \tag{14}$$

where $D(\theta)$ is directivity at beam steering angle θ and $D(0)$ is boresight directivity. Similarly, beam width for larger scan angle increases from boresight and can be approximated as

$$\theta_{\mathrm{HPBW}}(\theta) = \frac{\theta_{\mathrm{HPBW}}(0)}{\cos(\theta)} \tag{15}$$

where $\theta_{\mathrm{HPBW}}(\theta)$ is half power beam width (HPBW) at beam steering angle θ and $\theta_{\mathrm{HPBW}}(0)$ is boresight HPBW.

Scan loss of integrated lens antenna can be minimized by optimizing eccentricity [62]. When eccentricity of elliptical ILA equals to $e = 1/\sqrt{\epsilon_r}$ and extension length equals $L = e \cdot a$, it gives maximum boresight gain. In the optimization process, eccentricity of lens is optimized between 0 and $1/\sqrt{\epsilon_r}$ and also length of extension L is also optimized accordingly to achieve minimum scan loss. Eccentricity optimization is trade-off between boresight gain and scan loss. Reducing the eccentricity of an elliptical ILA reduces its boresight gain but also scan loss is minimized.

In literature [62], number of extended elliptical lenses of Rexolite ($\epsilon_r = 2.53$), diameter 100 mm, and different eccentricities were simulated to find optimum eccentricity. Optimum eccentricity is selected based on gain performance in large beam steering angles. Lens with eccentricity $1/\sqrt{\epsilon_r}$ and extension length, $e \cdot a$= 40.4 mm, gave 34.1 dB boresight directivity and 27.9 dB gain at 25° beam steering angle, resulting in 6.2 dB scan loss. Similarly, lens with eccentricity $0.78/\sqrt{\epsilon_r}$ and optimized extension length of 53 mm, gave boresight directivity of 30.8 dB whereas scan loss

was almost zero for ± 25°beam steering range.

Figure 10 illustrates ray presentation of the previously described losses in ILA. Irrespective of any form of loss in extension section, all rays going towards extension are considered as spillover loss. Red colored rays in Figure 10 below represents spillover loss. Green colored rays represent dielectric loss due to material dissipation while travelling from feed to collimating surface. Only rays reflected from collimating surface are considered as reflection loss as represented by pink colored rays. Blue rays are transmitted rays from collimating surface.

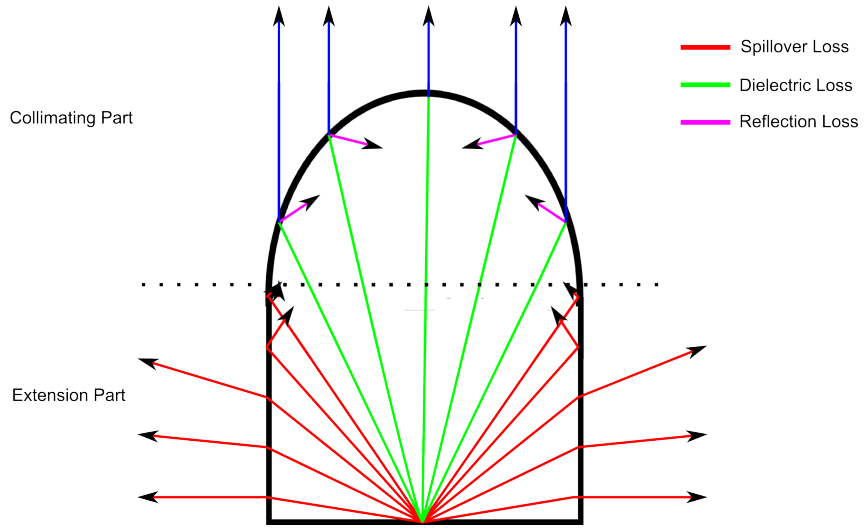

Figure 10: Ray presentation for different loss mechanisms in ILA: spillover loss (red), dielectric loss (green), reflection loss (pink), and transmitted rays (blue).

3.5 ILA Optimization Methods

3.5.1 Matching Layer

Reflection losses in ILA can be reduced by coating a quarter wavelength thick matching layer on lens-air interface [39]. Dielectric constant of such matching layer should be

$$\epsilon_{match} = \sqrt{\epsilon_1 \cdot \epsilon_2} \tag{16}$$

where ϵ_1 and ϵ_2 are dielectric lens permittivity and surrounding (air) permittivity respectively. As matching layer thickness depends on the operation frequency, it reduces bandwidth of ILA. In an experiment, at 60 GHz for $5{\cdot}\lambda$ wide and 7-mm thick flat dielectric lens of permittivity ϵ_r= 6, 1.2 dBi gain improvement was achieved with quarter wavelength matching layer of permittivity ϵ_{match}= 2.25. In another research [63], a comparison between lenses without matching layer, single matching layer and three matching layers was presented for extended hemispherical lens of diameter $5{\cdot}\lambda$ made from MACOR® (ϵ_r= 6) at center frequency of 28 GHz. Figure

11 (a) and (b) shows lens structural diagram of single matching layer lens and multiple matching layer lens. For the single matching layer lens, matching layer of (ϵ_r= 2.45) of thickness 1.71 mm is applied whereas for three matching layer lens, layers with permittivities ϵ_{r2}= 3.83, ϵ_{r3}= 2.45 and ϵ_{r4}= 1.56 of thickness 1.37 mm, 1.71 mm, and 2.14 mm respectively are applied. Results showed that both single matching layer and three matching layers had 18 % more power transfer through dielectric interface compared to lens without matching layer. Also, use of three matching layers enhanced radiation characteristics like beam symmetry and beam distortion over 36% of relative bandwidth.

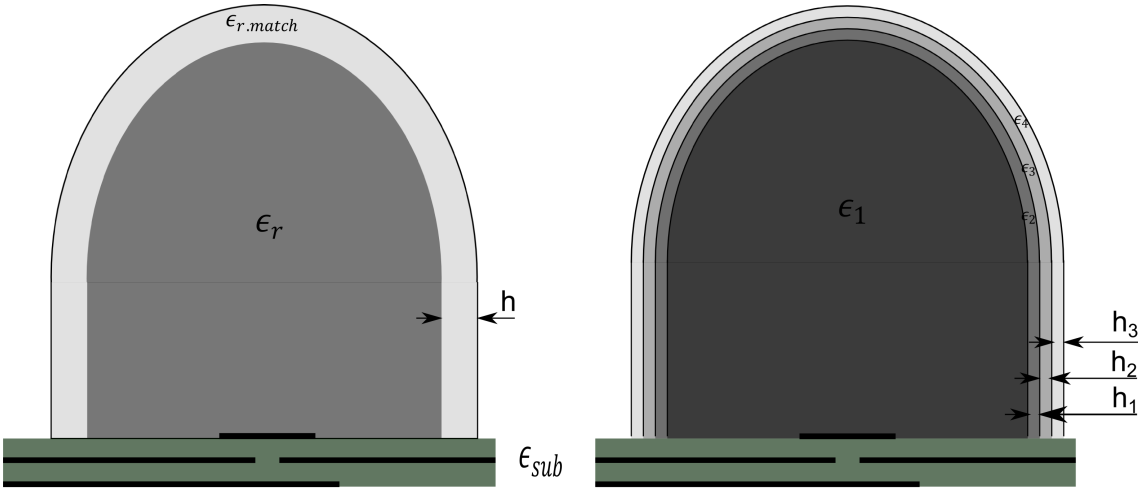

Figure 11: ILA with (a) single matching layer [39] and (b) multiple matching layer [63].

3.5.2 Double Shell Lens (DSL)

Significant amount of the loss in ILA is because of the reflection loss, though quarter wavelength matching layer minimizes it but that is a frequency dependent and limits bandwidth of dielectric lens. Double Shell Lens (DSL) antenna is shaped non-uniform indexed lens with high permittivity inner shell and lower permittivity outer shell [64]. Permittivity of outer shell is square root of inner shell i.e. $\epsilon_{r2} = \sqrt{\epsilon_{r1}}$. Main objective of such complex design is to reduce reflection loss and maximize efficiency of lens [64].

DSL with inner shell permittivity of ϵ_{r1}=5.5 and outer shell permittivity of ϵ_{r2} = 2.53, at 62.5 GHz had 85.37 % efficiency as compared to 67.49 % efficiency for hyper-hemispherical lens made of homogenous material of permittivity of ϵ_r=5.5 [65]. Both lens had the same physical dimensions. Geometry of double shell lens is depicted in Figure 12. DSL exhibited improved first side lobe level characteristic of -16.2 dB as compared to hyper-hemispherical lens with side lobe level of -10.04 dB. Detailed design procedure of DSL is illustrated in reference [64], where DSL was designed with MACOR® and acrylic as inner and outer shell materials respectively

had operation bandwidth is 40%. It exhibit gain scan loss of less than 1 dB for beam scanning range of ±20 °. Also reflection loss of less than 1dB is achieved. DSL can provide improved performance but it may encounter difficulties in the manufacturing perspective; it is difficult to find feasible materials for double shell having required dielectric properties and thermal properties. In previous example MACOR® and acrylic materials are used but dielectric constant of these material does not follow design rule $\epsilon_{r2} = \sqrt{\epsilon_{r1}}$ and loss tangent of both materials is ($\tan \delta = 0.0118$) which results in higher dielectric loss.

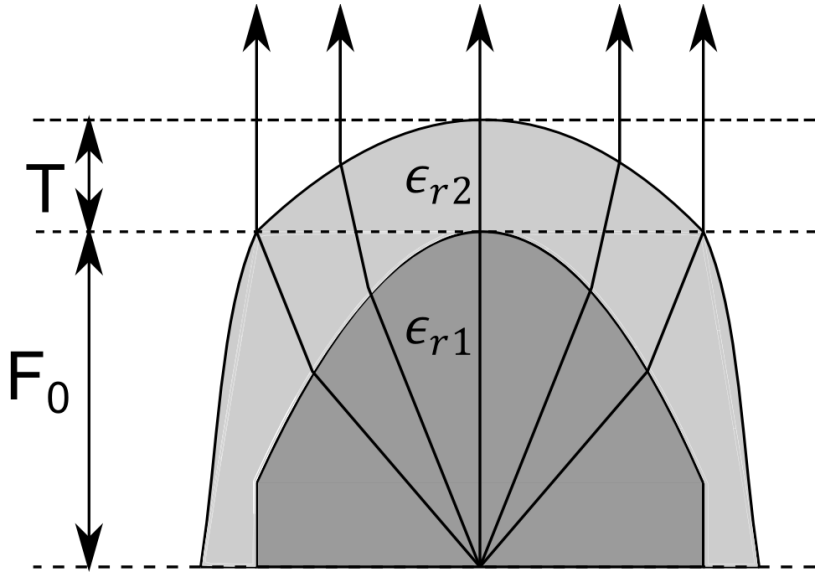

Figure 12: Double shell lens antenna schematics.

3.5.3 Zoning

The zoning is a process of removing dielectric material from lens of a thickness equal to an integer multiple of wavelength [39]. The zoning of lens helps to reduce weight, minimizes dielectric loss and possibly improve off-axis performance [66]. Thickness of each zoned volume is determined by relation

$$t = \frac{\lambda}{\eta - 1} \tag{17}$$

where t is zoning thickness, η is refractive index of lens material and λ is free space wavelength. Equation 17 implies that lens becomes frequency dependent after zoning. Bandwidth of zoned BW_{zl} lens can be estimated as

$$BW_{zl} = \frac{25\%}{K} \tag{18}$$

where K is the number of zones along the radius of lens [67]. Additional losses can be introduced because of scattering, diffraction effect and shadowing after zoning. An elliptical ILA with four spherical zones was designed with operating frequency

of 77 GHz to reduce weight of lens as shown in Figure 13 (b). Radius of spherical grooves is determined by relation

$$(R_i - R_{i+1}) \cdot (\sqrt{\epsilon_r} - 1) = \lambda_0 \tag{19}$$

where ϵ_r is material permittivity, λ_0 is free space wavelength and R_i and R_{i+1} are the radius of adjacent grooves [67]. Zoning helped to reduce weight by more than 70% and scan loss was limited to 1.5 dB for maximum 12° beam steering angle compared to 2 dB gain scan loss for elliptical lens, both made with teflon with dielectric constant ϵ_r =2.01 and loss tangent of tanδ=0.0003. Gain and side lobe level worsen after zoning of ILA and impedance bandwidth is 4.6 GHz, from 74.4 GHz to 79 GHz, for -10 dB matching. Also, side lobe level performance starts to worsen with small deviation from designed frequency due to frequency dependent hollow structure [67].

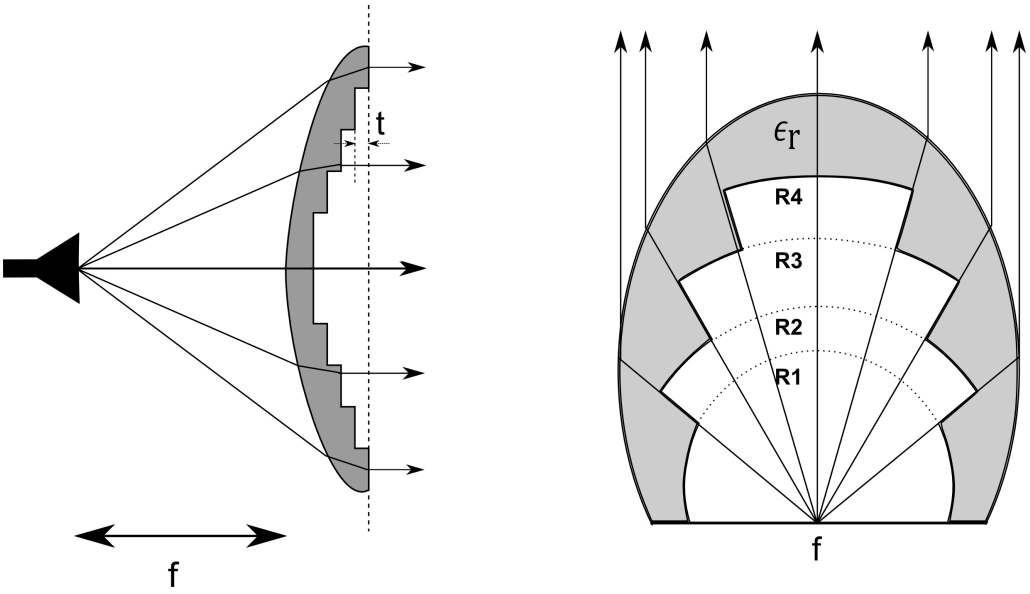

Figure 13: Zoning of (a) a hyperbolic lens [39] and (b) an elliptical lens antenna [67].

3.5.4 Double Lens (DL)

Double lens (DL) system is a combination of an immersion lens and an objective lens as shown in Figure 14. In reference [57], a plano convex objective lens and a hemispherical immersion lens of diameter 62.4 mm were made from Ultem ($\epsilon_r = 3.01$ and tan$\delta = 0.003$) material. Distance L between the objective and the immersion lens was optimized based on low scan loss and high boresight direcitvity performance criteria. In this design at $L/R = 0.72$, i.e $L = 22.5$ mm is used.

Characteristics of double lens system are compared with two extended hemispherical lens, first optimized for minimum scan loss, i.e. Ref. 1, and another extension optimized for maximum boresight directivity, i.e. Ref 2. Comparison results are shown in Table 2.

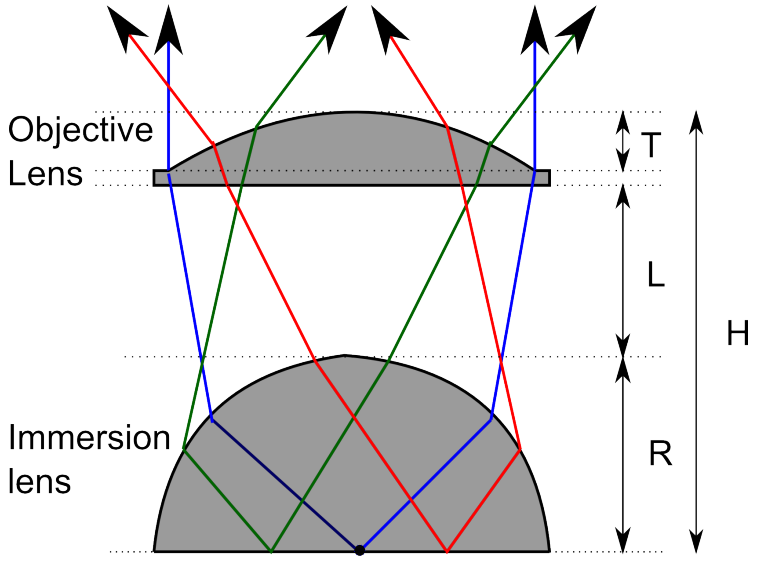

Figure 14: Double lens system and ray presentation [57].

Table 2: Performance comparison between the double lens antenna, two extended hemispherical lens (Ref. 1. and Ref. 2.) and an elliptical lens

Parameters	DL	Ref 1	Ref 2	Elliptical Lens
Diameter (mm)	62.4	62.4	62.4	62.4
Height (mm)	65.7	54.4	66	60.18
Weight factor	1	1.5	2.5	2
Boresight directivity (dBi)	31.2	28.7	32.2	33.6
Boresight gain (dBi)	28.7	25.6	28.7	29.4
Scan loss 30°(dB)	1.2	0.4	5.1	6.7
Radiation efficiency	56 %	49 %	45 %	
Aperture efficiency	53 %	30 %	66 %	
Total efficiency	30 %	15 %	30 %	37 %

3.6 Feed Antenna

Feed antenna is a source of radiation for a lens. The feeding antenna can be of any type but open ended wave-guides, horns, or patch antennas are commonly used. Study showed that edge illumination of level -10 dB compared to the central point gives the optimal gain performance in ILA [68].

Low profile nature and ease of integration with a RF circuit makes a microstrip patch antenna a viable option. Patch antennas are of narrow band but dielectric material in direct contact increase the bandwidth. Spurious feed radiation and high ohmic and dielectric loss at higher frequency are major disdavantages of patch antenna with microstrip lines feed [38]. Spurious radiation of a microstrip patch antenna can be reduced with an aperture coupled feed [69]. An aperture coupled microstrip antenna (ACMA) has theoretically zero cross polarization in priciple

planes that helps designing dual-polarized antenna. As the radiating patch and the feed lines are located in different substrate layers as shown in Figure 15 (a), it provides extra space for the radiating patch that helps to reduce coupling between the array elements and increase directivity. Additionally, the ACMA have larger impedance bandwidth, and enables independent selection of substrate material for feed lines and radiating patch. These properties of the ACMA make it a suitable feed option for the ILA.

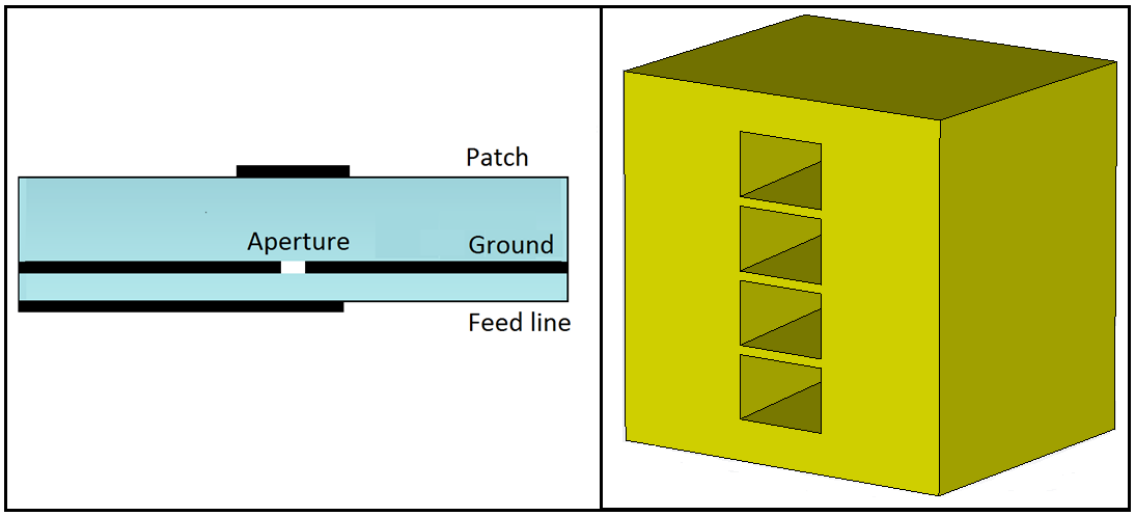

(a) (b)

Figure 15: (a)Aperture-coupled microstrip antenna and (b) horn array feed for ILA [70].

Planar aperture surface, low loss, and large impedance bandwidth makes a horn antenna suitable for the ILA feed source and also for a reflector antenna feed. Highly directive radiation characteristics of the horn makes it popular feed source for off body feed lenses [39]. Bulky shape and larger aperture area presents challenge in some application with specific requirements. Linear horn array is shown in Figure 15 (b). In addition to patches and horns, slot antennas and waveguides are also commonly used in different applications. Waveguide feed is specially utilized in prototype testing in lab due to its re-usability.

3.7 Summary

Design process of ILA is discussed in this chapter followed by performance optimization method. Elliptical ILA gives high boresight directivity but suffers from high scan loss. Losses in ILA depend on material permittivity, loss tangent and feed directivity. Various ILA performance optimization methods were discussed but their implementation requires careful approach due to design complexity, manufacturing constraints, bandwidth reduction and unavailability of material with desired dielectric properties.

4 Ray Tracing

4.1 Introduction

In optics, a very narrow beam of light is called a ray [71]. Ray tracing is a method of finding the path of an electromagnetic ray passing through regions of varying dielectrics, taking into account the absorption and reflection characteristics.

The exact behaviour of electromagnetic field is much more complex than that of rays, ray optics is asymptotic technique and its accuracy increases as frequency increases towards infinity and wavelength tend to zero or is extremely small compared to the dimension of the object with which the field interacts [72]. In high-frequency domain, full-wave methods like finite-difference time domain (FDTD), method of moment (MOM), finite element method (FEM) and spherical wave modal method have very high precision but are slow in analyzing electrically large structures and requires very high processing and memory capability. Therefore, ray tracing method is used in designing electrically large structures like lens and reflector antennas. Along with high frequency antenna design ray tracing has application in 3D imaging, channel propagation modeling, and computer graphics [73], [74].

4.2 Ray Tracing

Field due to given source can be decomposed to two parts amplitude and phase. Determination of the path helps to define the phase of the field whereas the determination of the intensity variation enables to calculate the amplitude of the field. In wave optics, amplitude and phase are intimately related.

Path of a ray can be traced with three simple laws: staight line propagation in homogenous region, the rule of reflection, and the rule of refraction [71]. When an incident ray hits dielectric interface with an incident angle of θ_i part of it is reflected and remaining is refracted. Let, $(\epsilon_{ri}, \mu_{ri})$ and $(\epsilon_{rr}, \mu_{rr})$ be permittivity and permeability pairs of dielectric boundary interface. Law of reflection states that the angle of reflection θ_r is equal to the angle of incidence, i.e $\theta_i = \theta_r$. The direction of refracted ray or transmitted ray follows Snell's law:

$$\sqrt{\epsilon_{ri}} \cdot \sin(\theta_i) = \sqrt{\epsilon_{rr}} \cdot \sin(\theta_t) \tag{20}$$

where θ_t is angle of refraction. Reflected and refracted ray directions are calculated using Snell's law and lens surface normal. Total reflection happens if the following criteria is met:

$$\begin{gathered} \epsilon_{ri} > \epsilon_{rr}, \text{and} \\ \theta_i \geq \sin^{-1}\left(\sqrt{\frac{\epsilon_{rr}}{\epsilon_{ri}}}\right) \end{gathered} \tag{21}$$

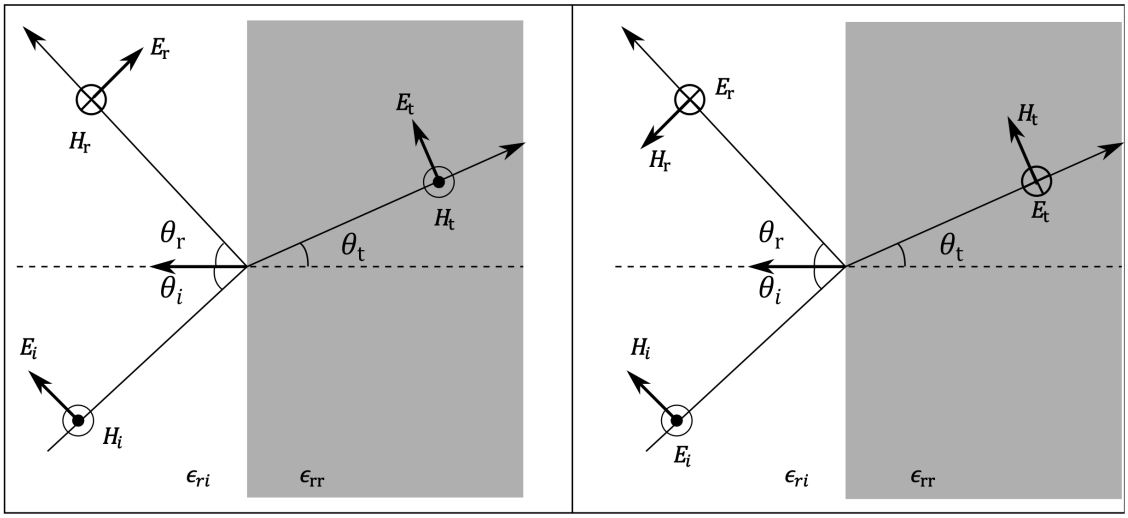

Figure 16: (a) Parallel and (b) perpendicular polarized waves in a dielectric interface.

Field across boundary is solved by dividing incident field vector E_i into parallel and perpendicular polarization components by dot product between incident electric field vector with perpendicular and parallel polarization vector respectively [18]:

$$\overline{E}_i^{\parallel} = (\overline{E}_i \cdot \overline{n}_i^{\parallel}) \cdot \overline{n}_i^{\parallel}, \qquad \overline{E}_i^{\perp} = (\overline{E}_i \cdot \overline{n}_i^{\perp}) \cdot \overline{n}_i^{\perp}, \tag{22}$$

Perpendicular polarization vector $\overline{n}_i^{\perp}$ is calculated with cross product calculation between surface normal vector and incident ray unit vector. Parallel $\overline{n}_i^{\parallel}$ polarization vector is calculated with cross product calculation between surface normal vector and perpendicular polarization vector $\overline{n}_i^{\perp}$. Reflection and transmission coefficient for parallel polarized waves are calculated with the following equations:

$$\Gamma_{\parallel} = \frac{\sqrt{\frac{\epsilon_{rr}}{\epsilon_{ri}} - \sin^2\theta_i} - \frac{\epsilon_{rr}}{\epsilon_{ri}} \cdot \cos\theta_i}{\sqrt{\frac{\epsilon_{rr}}{\epsilon_{ri}} - \sin^2\theta_i} + \frac{\epsilon_{rr}}{\epsilon_{ri}} \cdot \cos\theta_i} \tag{23}$$

$$\tau_{\parallel} = \frac{2 \cdot \sqrt{\frac{\epsilon_{rr}}{\epsilon_{ri}}} \cdot \cos\theta_i}{\sqrt{\frac{\epsilon_{rr}}{\epsilon_{ri}} - \sin^2\theta_i} + \frac{\epsilon_{rr}}{\epsilon_{ri}} \cdot \cos\theta_i}. \tag{24}$$

Reflection and transmission coefficient for perpendicular polarized wave are calculated with the following equations:

$$\Gamma_{\perp} = \frac{\cos\theta_i - \sqrt{\frac{\epsilon_{rr}}{\epsilon_{ri}} - \sin^2\theta_i}}{\sqrt{\frac{\epsilon_{rr}}{\epsilon_{ri}} - \sin^2\theta_i} + \cos\theta_i} \tag{25}$$

$$\tau_{\perp} = \frac{2 \cdot \cos\theta_i}{\sqrt{\frac{\epsilon_{rr}}{\epsilon_{ri}} - \sin^2\theta_i} \cdot \cos\theta_i}. \tag{26}$$

Finally, reflected field E_r and transmitted field E_t across boundary are calculated using

$$\overline{E}_r = \overline{E}_i^{\parallel} \cdot \Gamma_{\parallel} \cdot \overline{n}_r^{\parallel} + \overline{E}_i^{\perp} \cdot \Gamma_{\perp} \cdot \overline{n}_r^{\perp} \tag{27}$$

$$\overline{E}_t = \overline{E}_i^{\parallel} \cdot \tau_{\parallel} \cdot \overline{n}_t^{\parallel} + \overline{E}_i^{\perp} \cdot \tau_{\perp} \cdot \overline{n}_t^{\perp} \tag{28}$$

where $\overline{n}_t^{\parallel}$ and $\overline{n}_t^{\perp}$ are parallel and perpendicular polarization vectors of transmitted rays and $\overline{n}_r^{\parallel}$ and $\overline{n}_r^{\perp}$ are parallel and perpendicular polarization vectors of reflected rays. Perpendicular polarization vectors $\overline{n}_t^{\perp}$ of transmitted rays are calculated with cross product calculation between transmitted surface normal vector and transmitted ray unit vector. Parallel $\overline{n}_t^{\parallel}$ polarization vectors of transmitted rays are calculated with cross product calculation between transmitted surface normal vector and perpendicular polarization vector of transmitted ray $\overline{n}_t^{\perp}$.

Geometrical optics approximation does not represent change in amplitude of field but only phase change along the ray path is approximated. Wave-like properties of field are approximated by ray tubes and it helps in field and power calculation. A ray tube is a collection of elementary rays from the feed. A ray tube with four elementary rays is shown in Figure 17.

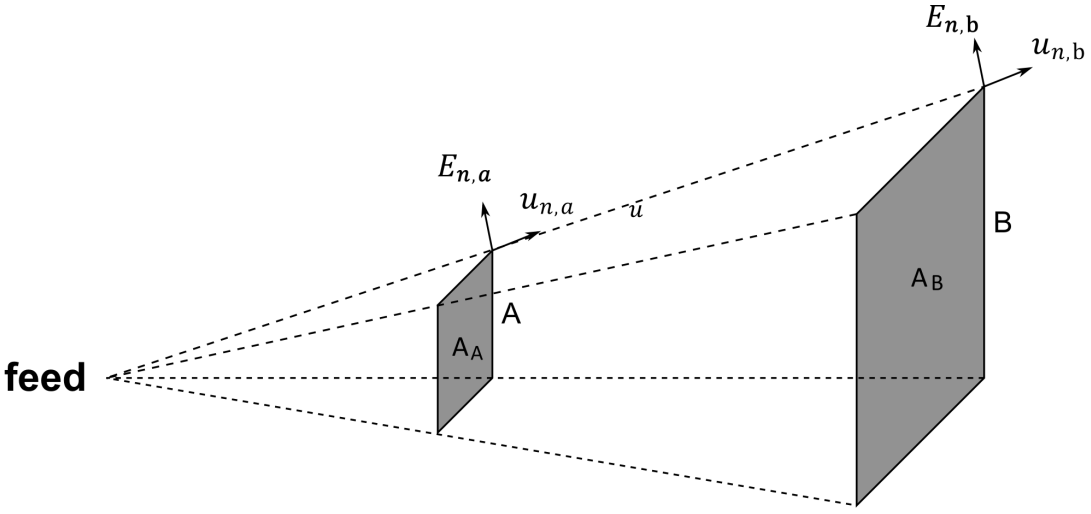

Figure 17: Ray tube presentation with four elementary rays.

Electric field change of nth ray that travels l distance between surface A and B is given by

$$\overline{E}_{n,B} = \overline{E}_{n,A} \cdot e^{-jk \cdot l} e^{-\frac{1}{2}\tan\delta \cdot k \cdot l} \tag{29}$$

where $\tan\delta$ is loss tangent of medium. Total field across surface B in a ray tube formed by N elementary ray is given by

$$\overline{E}_{B,tube} = \frac{1}{N} \sum_{N}^{n=1} \overline{E}_{n,b} \sqrt{\frac{A_A}{A_B}} \tag{30}$$

where A_A and A_B are cross section areas of tube perpendicular to direction of rays. Power at surface B of ray tube can be approximated as

$$P_{B,tube} = \frac{1}{2\eta} \left|\overline{E}_{tube}\right|^2 \cdot A_B \tag{31}$$

For a ray tube in lossless medium power at each cross section should be equal, i.e. $P_{B,tube} = P_{A,tube}$.

4.3 Lens Design with Ray Tracing

Simulated far-field radiation pattern of aperture coupled patch antenna designed by VTT is used as the feed source in ray tracing simulation. Directivity of feed antenna is 8 dB and the radiation pattern of the feed is shown in Figure 18.

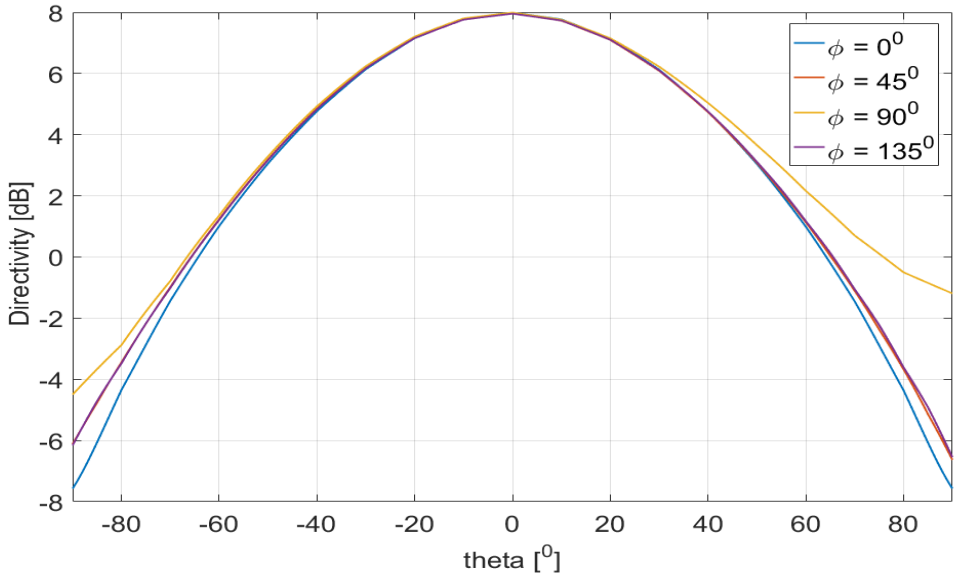

Figure 18: Directivity pattern of feed antenna.

Rays from the feed antenna are shot in equal angular interval and then Snell's law is used to trace rays propagation in the lens-air interface. Then, the calculated field outside the lens surface is transformed to far-field using aperture integration of equivalent surface currents. The equivalent electric $\overline{J_s}$ and magnetic $\overline{M_s}$ surface currents is calculated using tangential component of incident electric $\overline{E}$ and magnetic $\overline{H}$ field on the lens-air interface

$$\overline{J_s} = \overline{n} \times \overline{H} \tag{32}$$

$$\overline{M_s} = -\overline{n} \times \overline{E}. \tag{33}$$

In this simulation, the magnetic field $\overline{H}$ is calculated from the cross product of surface normal vector and electric field vector $\overline{E}$. Far-field transverse electric fields components are calculated by

$$\overline{E_\theta} \approx -\frac{jke^{-jkr}}{4\pi r}\left(\overline{L_\phi} + \eta\overline{N_\theta}\right) \tag{34}$$

$$\overline{E_\phi} \approx \frac{jke^{-jkr}}{4\pi r}\left(\overline{L_\theta} - \eta\overline{N_\phi}\right) \tag{35}$$

where k is the wavenumber, η is the free space wave impedance and r is the distance from lens surface to the point in the far field. The radiation integrals $\overline{N}$ and $\overline{L}$ are calculated as

$$\overline{N} = \iint_s^- \overline{J_s} e^{jkr'\cos\phi} ds' \tag{36}$$

$$\overline{L} = \iint_s^- \overline{M_s} e^{jkr'\cos\phi} ds' \tag{37}$$

where ds' is an elementary surface at the lens surface, r' is distance from feed to elementary surface area and ϕ is angle between r' and r.

The simulation does not consider losses in feed - in other words, a lossless feed is assumed. The design and optimization of the feed arrays are not in the scope of this thesis. Efficiency is important and the loss mechanisms in ILA should be known well. Losses in the lens are calculated as follows. Spillover loss is calculated as

$$L_{spill} = 10 \cdot \log_{10}\left(\frac{P_{tot}}{P_{hemi}}\right) \tag{38}$$

where P_{tot} is total power radiated by feed and P_{hemi} is power radiated by feed towards the collimating surface of the lens. It is important to note that all rays going to extension section are considered as spillover loss. Also, these rays in extension section are not considered during far-field calculation because they are going to be terminated with an absorber. Only the first order rays are taken into account, so the reflected rays possibly causing the increase in side lobe level are not taken into account.

Dielectric loss is calculated as

$$L_{dielec} = 10 \cdot \log_{10}\left(\frac{P_{hemi}}{P_{ir}}\right) \tag{39}$$

where P_{ir} is power incident in boundary of lens-air interface in collimating region of the ILA.

Reflection loss is calculated as

$$L_{refl} = 10 \cdot \log_{10}\left(\frac{P_{ir}}{P_{tr}}\right) \tag{40}$$

where P_{tr} is power transmitted from collimating surface (i.e. elliptical surface) towards air.

4.4 Summary

Lens antenna is electrically large structure, therefore ray tracing simulation is used to verify antenna characteristics. Theoretical background of ray tracing simulation was studied. Simulation results of ILA using ray tracing based MATLAB program will be shown in the following chapter.

5 Study of Lens Parameters

5.1 Introduction

In this chapter, results obtained from ray tracing simulation will be presented and explained. Term lens parameter indicates lens design parameters like diameter, permittivity, feed directivity, and feed position. Parameters such as gain, directivity, loss, XPD etc. that illustrate lens' performance are termed as lens characteristics. First, this chapter concentrates on establishing relation between various lens parameters and their impact on lens characteristics. Based on these relations, first ideal and later real lens parameters are chosen to meet regulation and specification mentioned in section 1.3.

5.2 Lens Dimension

In this section we will focus on determination of lens dimensions based on lens design parameters. Figure 19 shows variation in total height h in relation to lens diameter d and dielectric constant of the lens material. From Figure 19 (a) it can be seen that lens height increases linearly with increase in diameter. Total lens height is a sum of the major axis a of elliptical section and the length of the extension L. Based on design equation 9 and 47, major axis is directly proportional to minor axis, i.e. $b = d/2$ and length of extension is directly proportional to the major axis. Therefore, increase in lens diameter leads to increase in both major axis and length of extension and consequently height of the lens increases.

Figure 19 (b) shows the simulated result of the lens height with respect to the permittivity of the material used in lens. The lens height decreases with the higher permittivity of the material. Based on 47, higher permittivity results in decreased eccentricity of lens, which in turn decrease the length of extension and major axis, resulting in a smaller lens height.

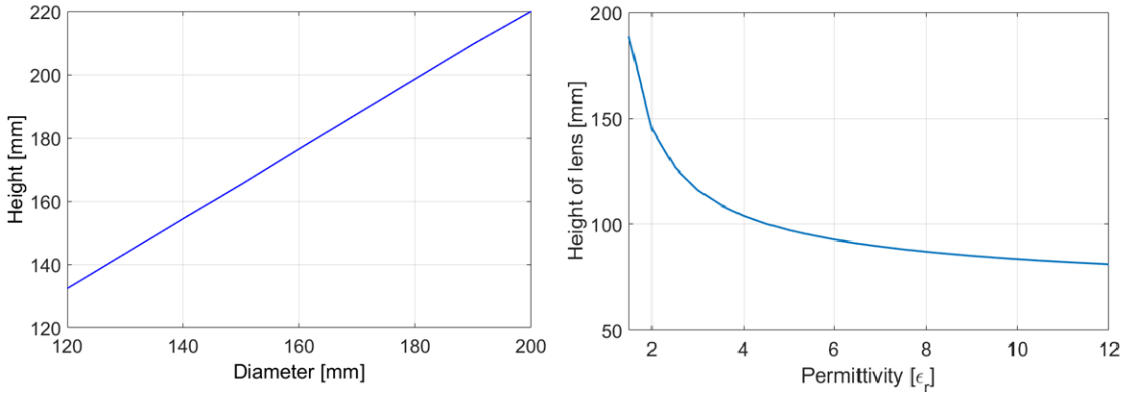

(a) (b)

Figure 19: Change in the lens height with respect to (a) diameter ($\epsilon_r = 2.3$) and (b) permittivity ($d = 120$ m).

5.3 Lens Characteristics

This section will emphasize the relation between lens design parameter and lens characteristics (i.e. directivity, gain, loss, radiation pattern, cross polarization level and side lobe level), which would help to understand lens performance. Beam steering property of lens antenna will also be demonstrated.

5.3.1 Diameter

In Figure 20 (a), the relation between the directivity, gain and diameter is shown for HDPE material (ϵ_r = 2.3, tanδ=0.0003) [19] and it can be deduced that the directivity is proportional to the diameter of a lens. Increase in the diameter makes aperture surface area larger and the directivity increases. There is no significant change in the lens losses with the varying diameter, as depicted in Figure 20 (b). There is a slight increase in the total loss caused by the increase in the dielectric loss, whereas spillover and reflection losses is constant over entire range of diameter. Increase in the dielectric loss is because lens dimension gets bigger with diameter, producing more dielectric losses in the lens.

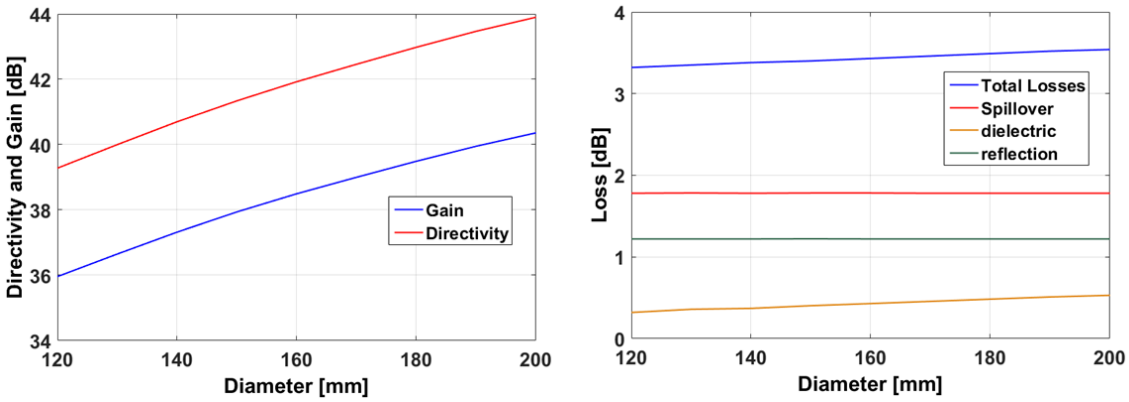

(a) (b)

Figure 20: (a) Directivity and gain and (b) loss relation w.r.t. diameter for an elliptical HDPE (ϵ_r=2.3, tanδ=0.0003) lens.

5.3.2 Feed Position

The beam steering property of ILA based on a HDPE lens with 120 mm diameter is shown in Figure 21. With the increasing feed offset position, the main beam of the lens antenna is steered further away from the lens axis as shown in Figure 21 (a). Also, with the increasing beam steering angle the half power beam width (HPBW) becomes wider as shown in Figure 21 (b). Directivity decreases and losses increases with higher beam steering angle as shown in Figure 21(c) and (d). Increase in reflection loss in collimating surface as shown in Figure 21 (d) and 22, is the main reason behind the drop in the gain.

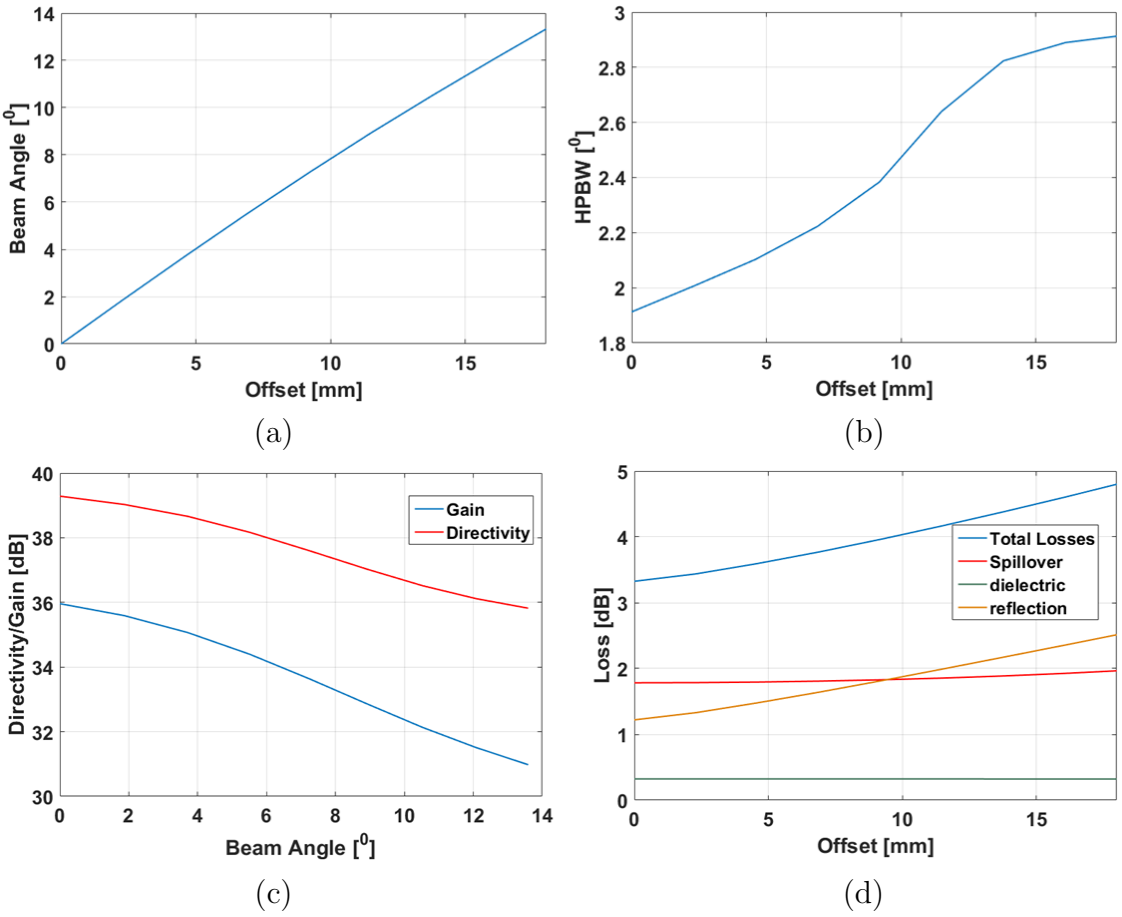

Figure 21: (a) Beam steering angle, (b) HPBW, (c) directivity and gain, and (d) loss performance analysis w.r.t. feed antenna offset position for a 120 mm HDPE (ϵ_r =2.3, tanδ=0.0003) lens.

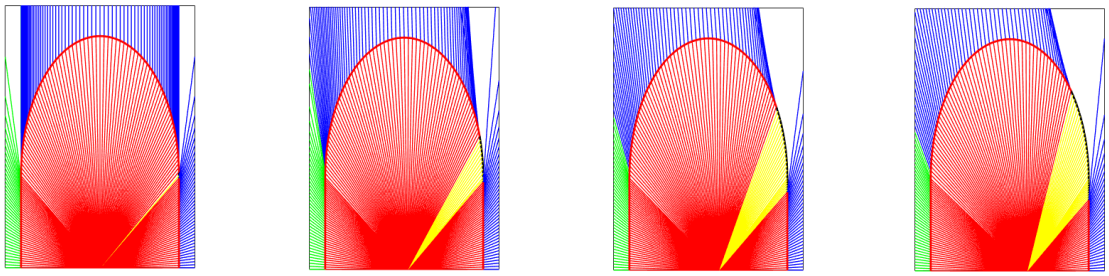

(a) (b) (c) (d)

Figure 22: Ray plots of 120 mm lens at various feed offsets (a) 0 mm, (b) 4.6 mm, (c) 13.08 mm, and (d) 23 mm; incident rays (red), totally reflected ray (yellow) and transmitted rays (blue and green).

5.3.3 Permittivity

After analyzing the beam steering properties, the lens characteristics were evaluated with real materials that have contrasting permittivity and loss tangent values as given in Table 3. The total lens height for these real materials with a 120 mm lens diameter is presented in Table 3, which support previous result in section 5.1 that the lens height reduces with increasing material permittivity. Figure 23 (a) illustrates that with higher permittivity material main beam is directed further away from boresight as compared to low permittivity material for the same offset position. At 10 mm feed offset position germanium (ϵ_r=16.1) gives 28° beam angle compared to 7.7° for HDPE material (ϵ_r=2.3). Therefore, maximum offset required for 10° beam steering angle reduces with increasing permittivity as shown in Figure 23 (c). Similarly, maximum distance between feed antennas required to maintain 3 dB beam overlapping in far field reduces. Decrease in antenna spacing will effect coupling between feed antennas and feed directivity. Therefore, minimum distance between feed elements required to maintain low coupling may limit material (permittivity) selection. The feeding network may also limit the placement of antenna elements.

Table 3: Dielectric properties of some materials at millimeter waves and the height of a 120 mm diameter lens.

Material	Permittivity	Loss Tangent	Frequency (GHz)	Temperature (K)	Height(mm)
HDPE (polyethylene) [70]	2.3	0.0003	73.5	300	132.4
Quartz Crystalline [75]	4.6	0.00001	245	300	99.44
Alumina [75]	9.4	0.0017	100	300	84.4
Germanium [75]	16	0.0001	150	300	77.46

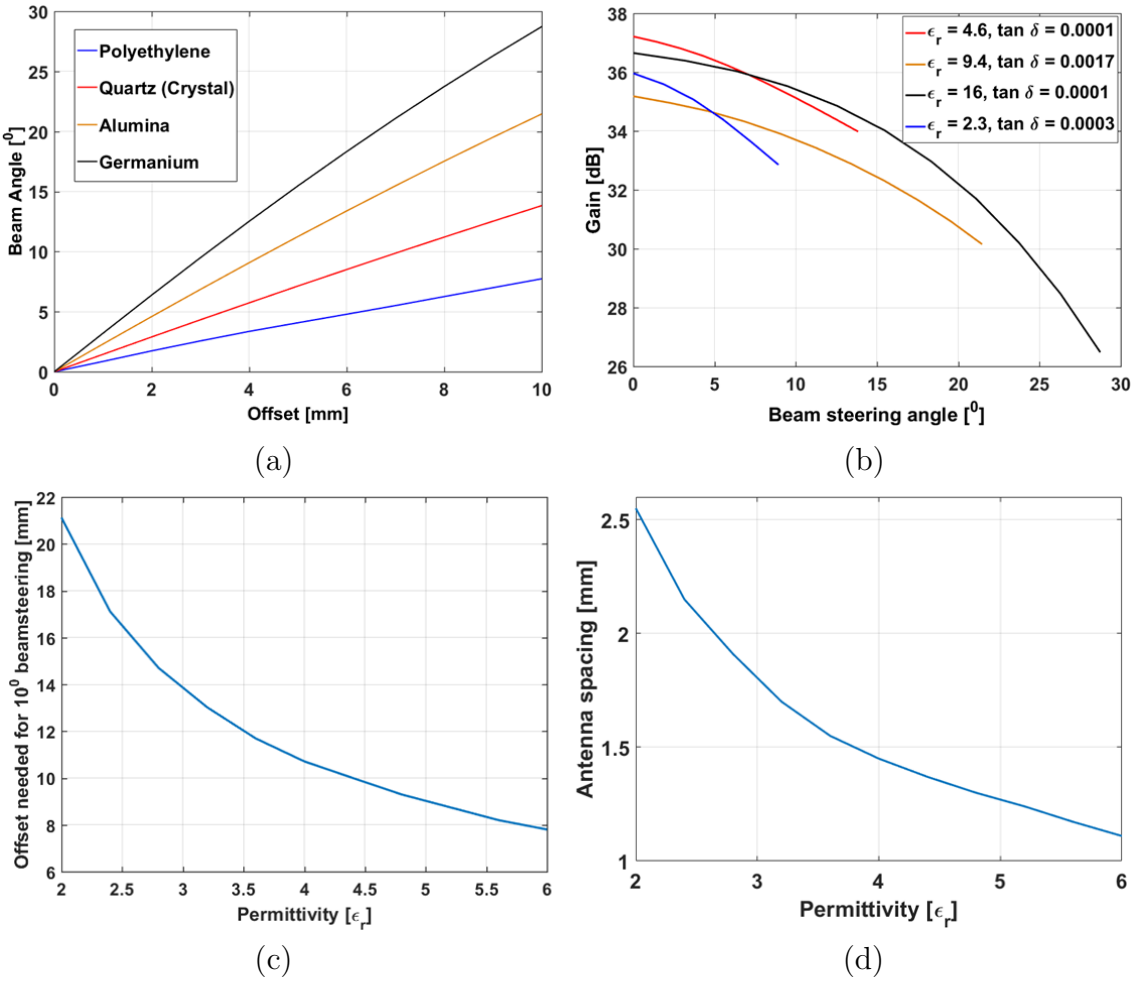

Figure 23: (a) Beam steering angle, (b) gain, (c) offset required for 10° beam steering, and (d) antenna spacing for 3 dB beam overlapping w.r.t varying permittivity for a 120 mm lens.

Figure 24 (a) shows the total loss of materials mentioned in Table 3. The total loss in a lens antenna depends upon loss tangent and dielectric constant of the material used. In Figure 24 (b), reflection losses for these materials are analyzed and material with higher permittivity is found to have more reflection loss than low permittivity material. Bigger difference in dielectric constant in lens-air interface gives higher reflection coefficient, resulting in higher reflection loss. It is also important to notice that reflection loss starts to increase towards higher offset position due to total internal reflection of rays as depicted in Figure 22. Figure 24 (c) shows that high permittivity materials have low spillover loss compared to low permittivity material. High permittivity material have small extension length, therefore the spillover loss is small. The dielectric loss depends upon loss tangent of lens material. Higher loss tangent means higher dielectric loss and vice versa. Figure 24 (d) confirms the same proposition. Alumina with loss tangent of tanδ= 0.0017 have the highest dielectric loss.

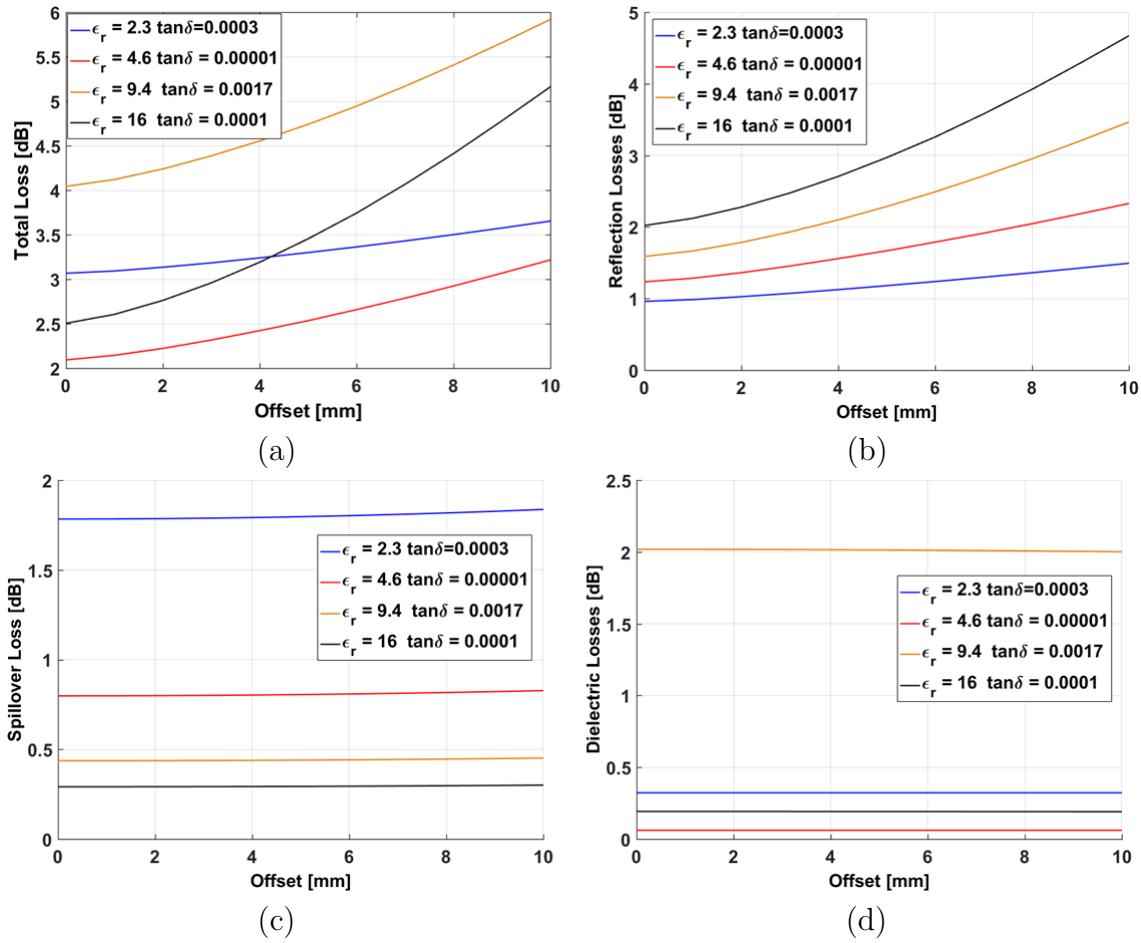

Figure 24: Loss analysis for different materials: (a) total loss, (b) reflection loss, (c) spillover loss, and (d) dielectric loss of a 120 mm diameter lens.

5.3.4 Feed Directivity

The effect of the feed radiation pattern is illustrated in this section. Point source feed radiation pattern

$$E(\phi, \theta) = cos^N(\theta), \quad \text{where} \quad 0 < \theta < 90^0, 0 < \phi < 360^0 \tag{41}$$

with Ludwig's second definition of polarization is considered for simulation [76]. Directivity of the source varies with parameter N. In this analysis, parameter N is varied from 0 to 10, consequently the directivity is varied from 3.0 dB to 16.1 dB. Figure 25 (a) shows variation in the lens directivity and gain w.r.t. the feed directivity of the HDPE lens with three different lens diameters, i.e. 120 mm, 160 mm, and 200 mm. With increasing feed directivity, lens directivity increases slightly because more power reach aperture surface with more directive feed. After a limit the directivity of the lens reduces due to under illumination of the collimating surface by a

narrow beam. As feed radiation pattern becomes directive, more power is incident on collimating surface and spillover loss decreases, consequently loss decreases and gain increases. Figure 25 (b) demonstrates the total loss with the varying feed directivity.

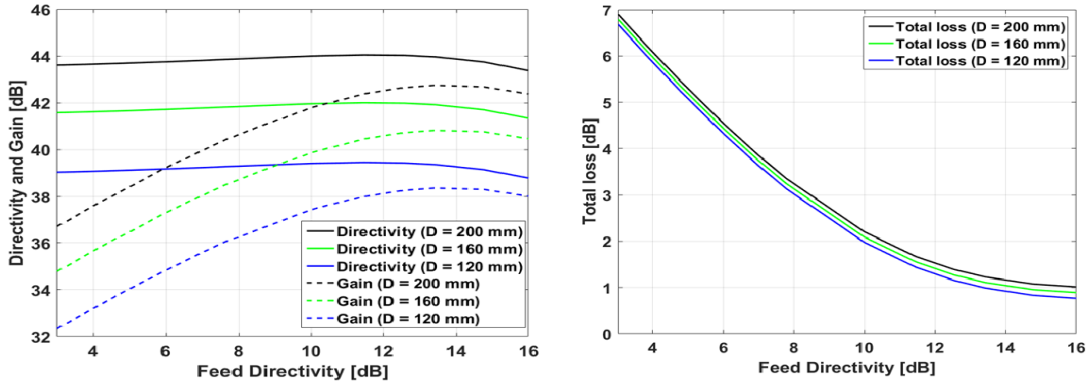

(a) (b)

Figure 25: (a) Directivity and gain and (b) loss performance of a HDPE lens w.r.t. feed directivity.

Overall loss of 160 mm HDPE lens is illustrated in Figure 26 (a), and it can be deduced that high directivity feed antenna have lower losses because of decrease in amount of spillover and reflection losses. Further simulations were done to understand the effect of the feed directivity on the scan loss performance. The HDPE lens with 160 mm diameter was simulated to achieve the beam steering angle up to 10° with three different feed directivities. Figure 26 (b) shows 5 dB, 4.1 dB, and 3 dB gain scan loss to feed directivity 3 dB, 10 dB, and 16.1 dB respectively for 10° beam steering. The gain scan loss for 10° beam steering angle is 5.9 dB, 4.37 dB and 2.87 dB for feed directivities of 3 dB, 10 dB and 16 dB respectively.

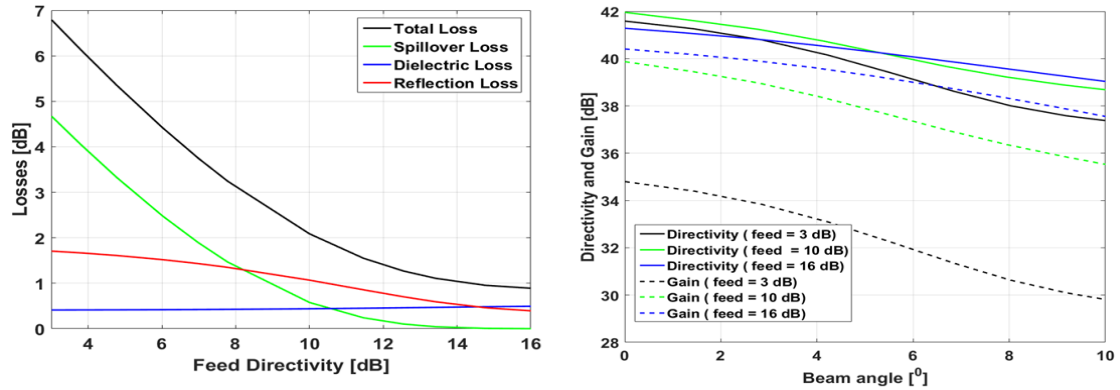

(a) (b)

Figure 26: (a) Loss analysis of a 160 mm diameter HDPE lens and (b) directivity and gain comparison for various feed directivities w.r.t. the beam angle.

5.4 Lens Optimization

This section focuses on finding the optimum values of lens parameters to achieve given targets described in section 1.3. First, a parametric sweep of permittivity was done to obtain feasible values for the lens. Later, the eccentricity optimization method is demonstrated which helps to reduce the scan loss.

Figure 27 (a) shows result of the parametric sweep of permittivity between $1.1-9$ and loss tangent between $0.01-0.00001$ for 120 mm diameter lens. Reasonable loss tangent of $\tan\delta = 0.0006$ was used to study losses in the entire permittivity range as shown in Figure 27 (b) which helps to understand gain characteristics. The result shown in Figure 27 (b) suggest that at lower permittivity the spillover loss is very high which decreases gain. As the permittivity increases spillover decreases but the reflection loss starts to increase, therefore the overall loss does not change much for the higher permittivity.

These simulations help to conclude that material with permittivity between $3-5$ and loss tangent less than 0.001 is recommended for a high gain performance for the lens antenna.

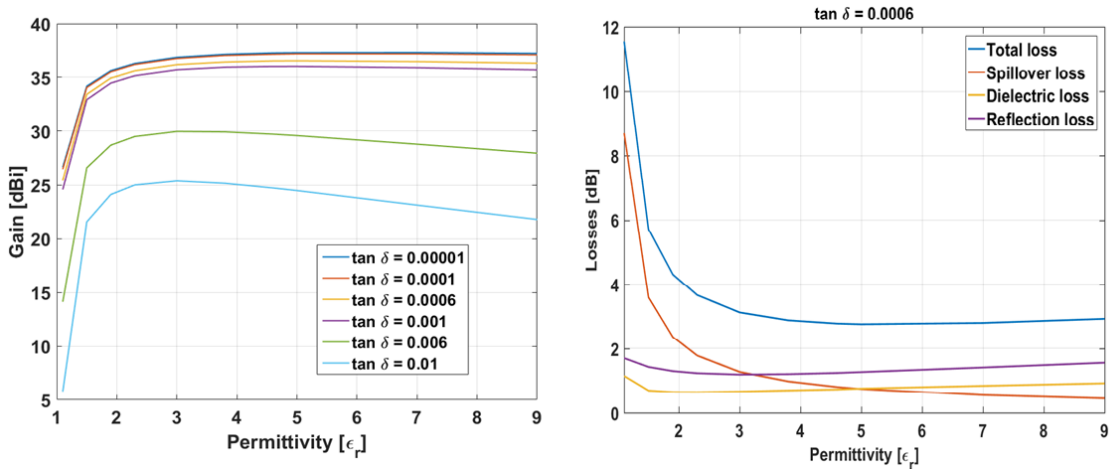

(a) (b)

Figure 27: (a) Gain and (b) loss for permittivity sweep for 120 mm lens diameter.

For the elliptical lens the boresight directivity and gain is maximum for eccentricity $1/\sqrt{\epsilon_r}$, but the scan loss is also high for the offset positions, therefore gain criteria for large beam steering angle is not easy to meet. Eccentricity optimization method is used as a tradeoff between the boresight gain and scan loss to meet the given criteria. Figure 28 (a) shows result of eccentricity optimization for a Quartz lens with 160 mm diameter. With eccentricity of $1/\sqrt{\epsilon_r}$, extension length $L = 47.8$ mm and total lens height of $h = 141$ mm, the boresight gain is 38.8 dB and the gain scan loss is 5.5 dB for 10° beam steering angle. A lens with eccentricity of $e = 0.8/\sqrt{\epsilon_r}$ and optimized extension length of $L = 60$ mm and total lens height h

= 147.4 mm have lower boresight gain of 36.8 dBi, but the scan loss is less than 1 dB. In the eccentricity optimization, the boresight gain is compromised to achieve a better gain performance in larger beam steering angles.

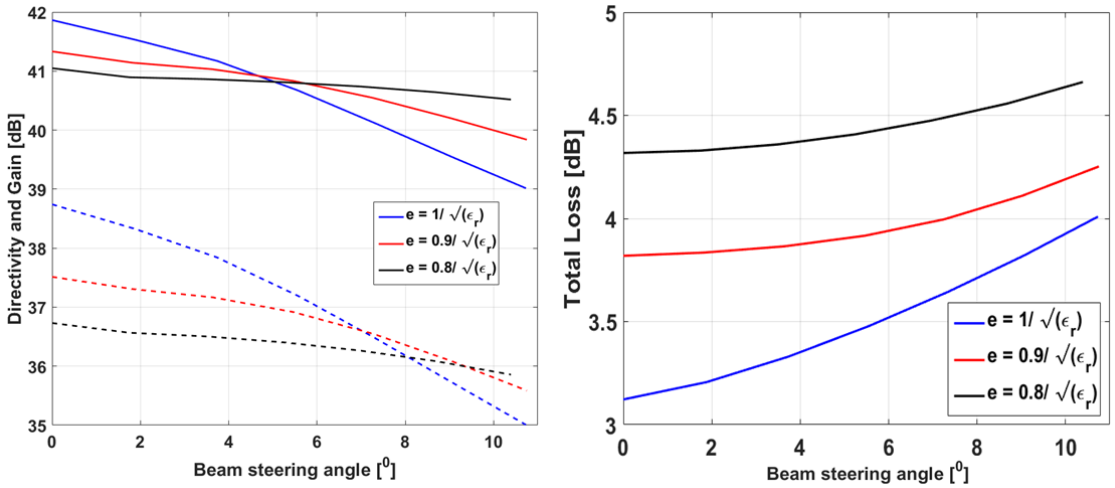

(a) (b)

Figure 28: (a) Directivity and gain, and (b) total loss result of a Quartz lens (ϵ_r =3.8 and tanδ = 0.0006) of 160 mm diameter with three different eccentricities.

5.5 Lens Material Study

In section 5.3, lens characteristics were studied with real materials having contrasting dielectric properties. This section presents real materials that have dielectric properties close to recommendation of section 2.3. Table 4 illustrates list of such materials. Gain performances of lenses made of materials mentioned in Table 4 are shown in Figure 29. Considering the HDPE lens as baseline, materials resulting in lens gain characteristics worse than those of HDPE are removed in Figure 30 (a) and (b). Figure 30 (a) shows that crystalline quartz, fused silica, and boron nitride materials have better performance than HDPE. Based on preliminary literature survey, these materials are commercially available, but their applicability in terms of lens manufacturing aspects i.e. size, shaping, cost etc. is yet to be studied.

Table 4: Real materials with dielectric properties at millimeter wave

Material	Permit-tivity	Loss Tangent	Frequency (GHz)	Temperature (K)	Attenuation factor(dB/cm)
Quartz crystal [75]	4.40	0.00051	140	300	0.136
Fused Silica [77]	3.81	0.00055	150	300	0.146
Boron Nitride [78]	4.20	0.00064	245	300	0.292
Fluorosint [79]	3.50	0.0017	150	300	0.433
HDPE [70]	2.30	0.0003	73	300	0.030
Nylon [80]	2.99	0.00088	100	300	0.138
Macor [81]	5.60	0.0015	100	300	0.322
Rexolite [53]	2.53	0.0013	73	300	0.137

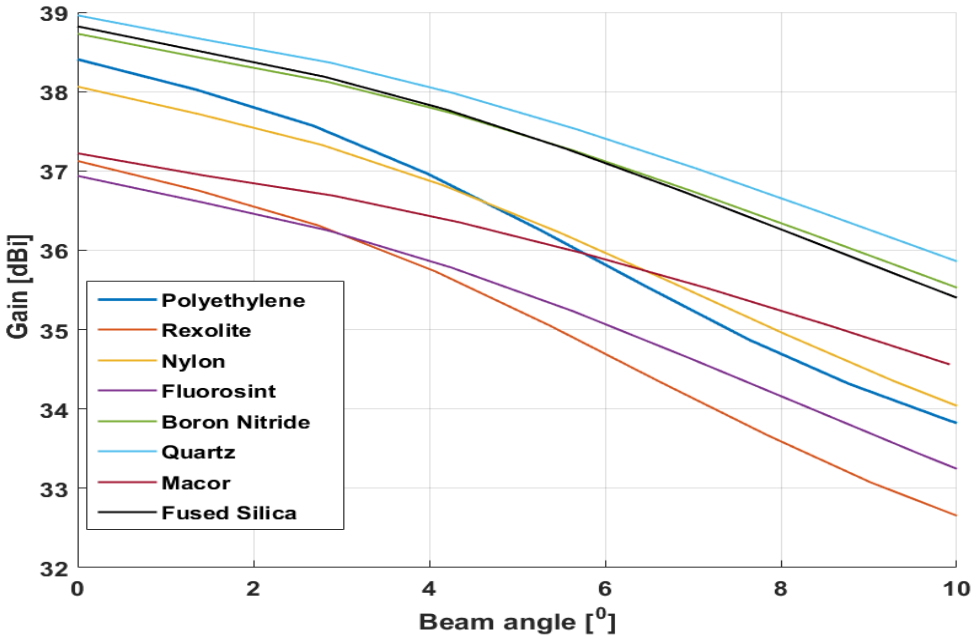

Figure 29: Gain of 160-mm diameter lens realized with different real materials w.r.t. beam angle.

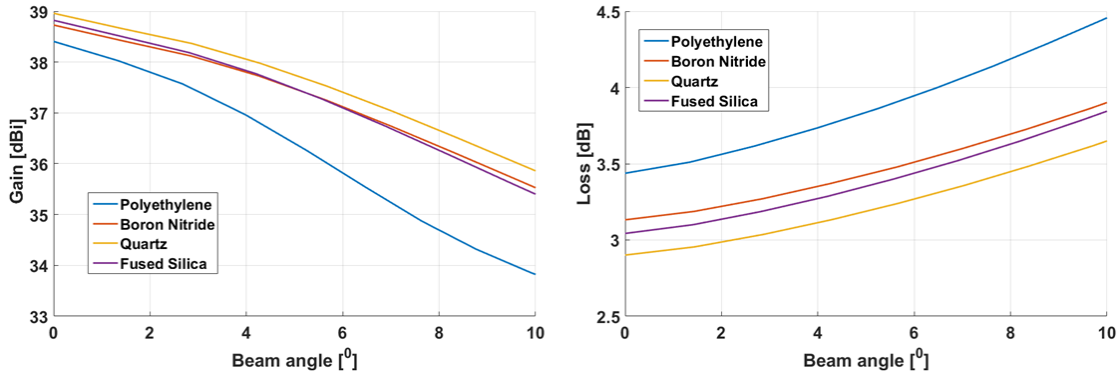

(a) (b)

Figure 30: (a) Gain and (b) loss performance of selected materials w.r.t. beam angle for 160 mm lens diameter.

5.6 Lens Designs

5.6.1 PREPERM ® L450 Lens

In section 5.4, we concluded that material with dielectric constant between 3-5, would best suit for high gain lens antenna. PREPERM® L450 material from Premix Oy with dielectric constant of 4.5 and loss tangent of 0.0046 [82] seemed most suitable because it is commercially available and material is also suitable for injection molding which would be helpful in mass manufacturing process. As shown in Figure 31 (a) and (b), directivity and losses increase with lens diameter. Attenuation factor of material is 0.644 dB/cm, therefore the rate of increase of dielectric loss exceeds rate of increase of directivity after a certain lens diameter, i.e. 200 mm. Therefore, it is not possible to increase the gain beyond 32.25 dBi at 200 mm diameter by increasing lens diameter further.

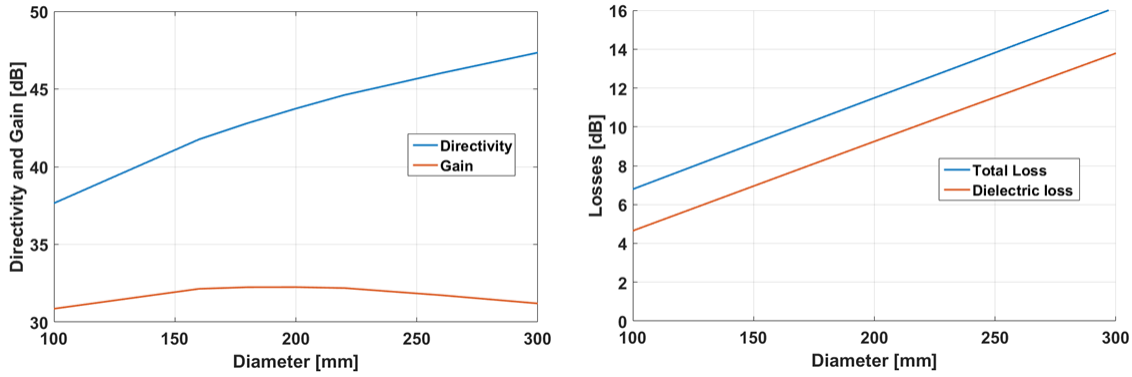

(a) (b)

Figure 31: (a) Directivity and gain and (b) loss performance of PREPERM® L450 lens.

5.6.2 Proposed Lenses

This section proposes two lens designs based on results of previous section. Since PREPERM®L450 has high loss tangent, it is not possible to meet the given gain specification. Commercially available HDPE (High-density Polyethylene) material is used in both proposed lenses in this section. Permittivity of HDPE is not in the recommended range given in section 4.3 which implies for high spillover loss. Low loss tangent tan$\delta = 0.0003$ of HDPE minimizes dielectric loss. Therefore, better performance is achieved with HDPE material instead of PREPERM® L450 material. Aperture coupled patch antenna designed by VTT with directivity 8 dB is used as feed source for ray tracing simulation while designing these lens.

First, a lens was designed with HDPE material to meet boresight gain criteria of 38 dBi. Specific values for the lens parameters are given in Table 5 and lens characteristics are given in Table 6. Then, the second lens was designed with HDPE material to meet the gain specification up to 5° beam steering angle. In comparison to first lens, the lens size has increased and eccentricity has been optimized. The designed lenses are called First Lens and Second Lens respectively. Specific values of lens parameters are given in Table 5 and lens characteristics are given in Table 6.

Table 5: Lens parameters of the proposed lenses.

Lens	Permittivity (ϵ_r)	Loss tangent (tanδ)	Eccentricity factor	Diameter (mm)	Lens height (mm)	Feed offset for 10° (mm)
First Lens	2.3	0.0003	1	160	177	18
Second Lens	2.3	0.0003	0.95	210	236	24

Table 6: Lens characteristics of the proposed lenses.

Characteristics	First Lens			Second Lens		
	Boresight	5°	10°	Boresight	5°	10°
Directivity (dB)	41.84	40.17	38.25	43.8	42.9	40.5
Loss (dB)	3.43	3.85	4.47	4.71	4.71	5.03
Gain (dBi)	38.4	36.35	33.7	39.13	38.22	35.47
Cross polarization level (dB)	-27.15	-27.24	-27.59	-30.46	-28.77	-26.19

First Lens

Lens characteristics with respect to the feed offset position and beam steering angle are shown in Figure 33. Specification for the gain is met at boresight position but at higher beam steering angle criteria is not met. Cross polarization level (XPD)

is below -27 dB for the entire beam steering range. Boresight radiation pattern of First Lens fits Radiation Pattern Envelope (RPE) criteria as shown in Figure 32.

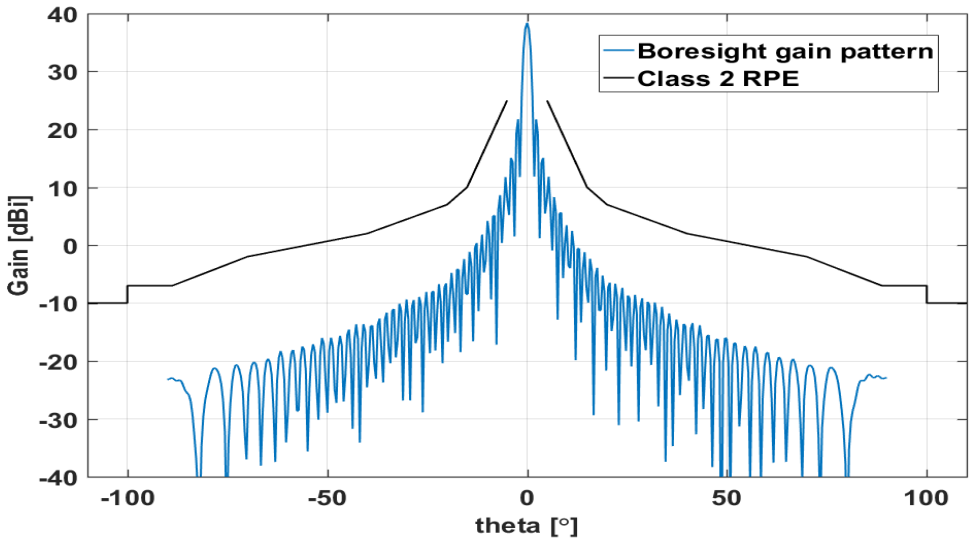

Figure 32: Boresight radiation pattern of First Lens with class 2 RPE.

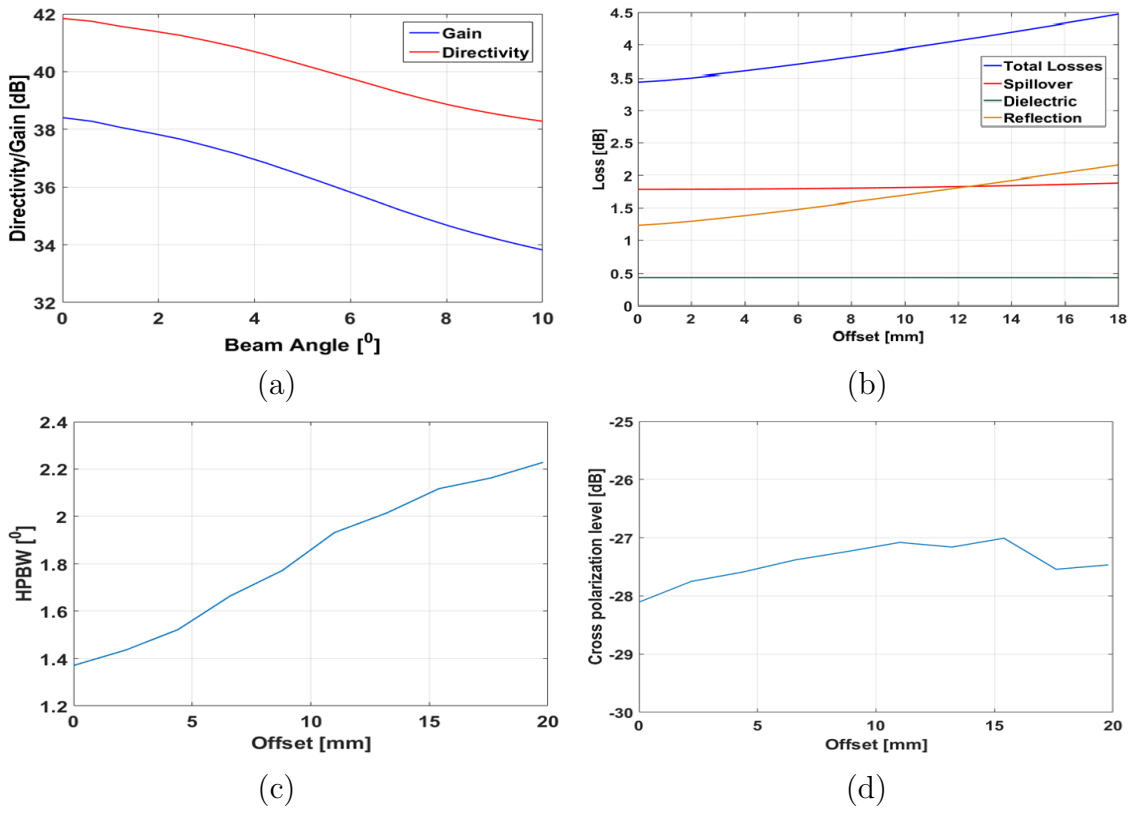

Figure 33: (a) Directivity and gain, (b) loss, (c) HPBW, and (d) cross polarization level characteristics w.r.t. offset or beam steering angle for the 160 mm HDPE lens.

Second Lens

Lens characteristics with respect to offset position and beam steering angle are shown in Figure 35. Specification for the gain is met at boresight and 5° beam steering angle but at higher beam steering angle criteria is not met. Figure 34 shows gain radiation pattern for boresight, 5° beam angle and 10° beam angle. Cross polarization level (XPD) is below -26 dB for the entire beam steering range.

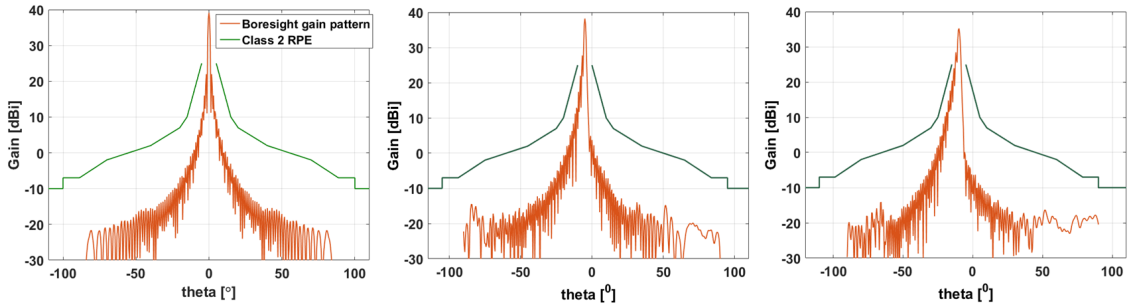

(a) (b) (c)

Figure 34: Radiation pattern with class 2 RPE for (a) boresight, (b) 5° beam angle (c) 10° beam angle of Second Lens.

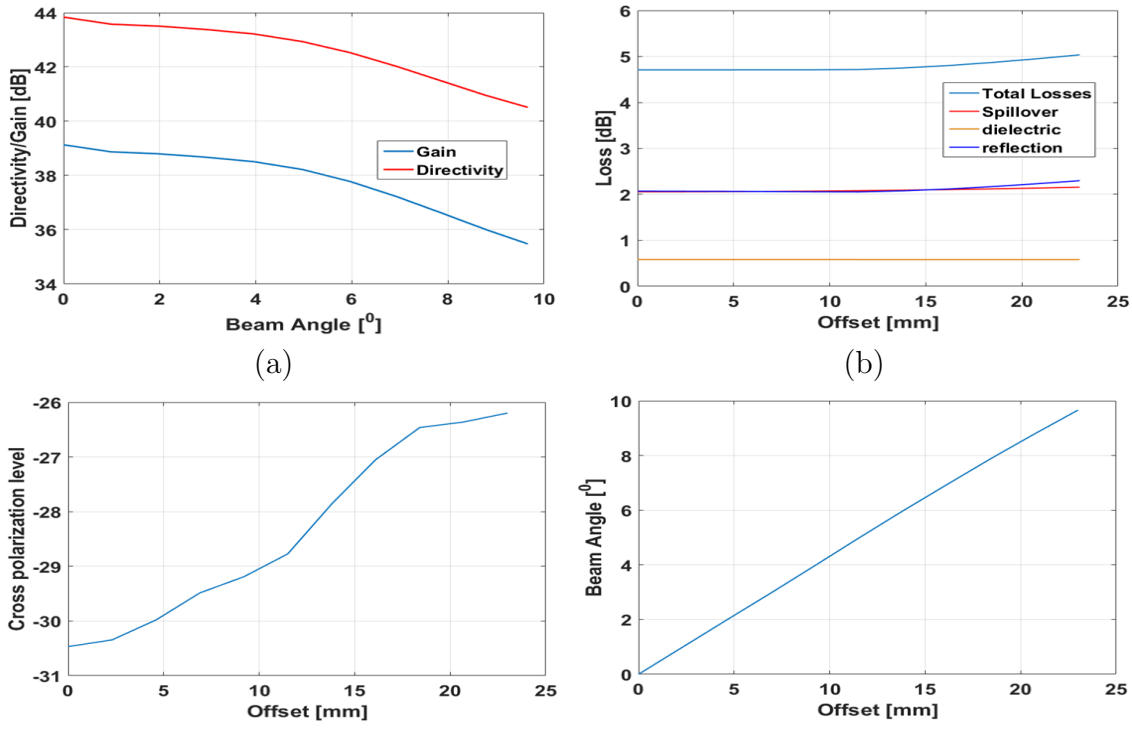

(a) (b) (c) (d)

Figure 35: (a) Directivity and gain, (b) loss, (c) HPBW, and (d) cross polarization level characteristics w.r.t. offset or beam steering angle for Second Lens.

5.6.3 ILA Extension Design

Main objective of designing grooves along the extension is to minimize reflection from the extension so that the reflected rays have minimum effect upon the radiation pattern. In order to ensure minimum reflection and maximum transmission through the extension grooves are designed in such a way that the angle of incidence of the ray is as small as possible at the lens surface. Design of extension length also helps to attach PVC absorber to lens. First Lens with optimized grooves is shown in Figure 36 (a).

Figure 36 (b) shows the comparison of the reflection performance of the lenses with and without grooves in the extension. Near the boresight, reflection from the extension is almost equal in both cases but with higher steering angles the effect is visible. At 10° beamsteering angle the grooved lens have approximately 0.5 dB better performance compared to the lens without grooves.

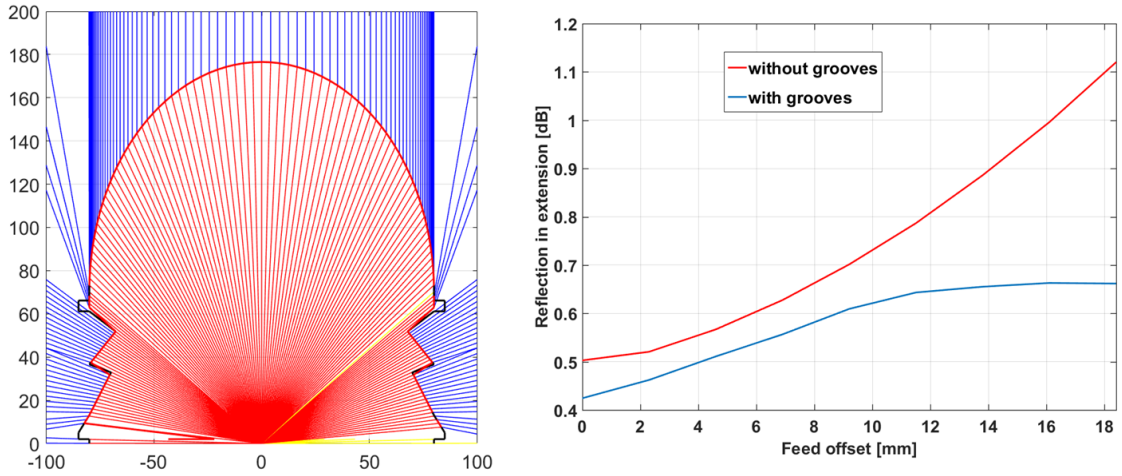

(a) (b)

Figure 36: (a) First Lens with grooves in the extension and (b) comparison of the reflected power from extension with and without grooves.

5.7 Trade-off Analysis between Lens Size and Beam Steering Angle

Studies in the previous section shows that the lens gain is directly proportional to its diameter. Increasing the dimensions of the lens helps to meet the gain criteria at higher beam steering angles but with the manufacturing and application perspective bigger lenses are challenging. Therefore, a trade-off analysis is done between the lens dimension and the beam steering angle to find suitable value for the application purpose.

Table 7 and Figure 37 (a) and (b) show the diameter and height variation for different lenses, capable of beam steering starting from the boresight up−to 5° . Diameter and height is optimized to meet 38 dBi gain specification at the given beam steering angle. Lens dimensions for elliptical lenses and eccentricity optimized lenses are depicted. Up−to a certain beam steering range, i.e. about 3° , eccentricity optimization method is not feasible because the boresight gain (or maximum gain) is close to 38 dBi and change in the eccentricity would degrade the boresight gain such that the given specifications are not met.

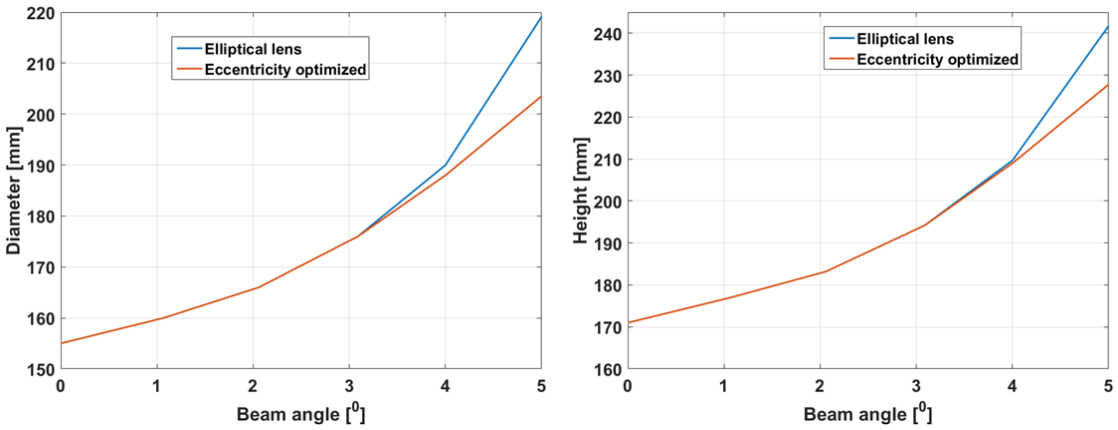

(a) (b)

Figure 37: (a) Diameter and (b) height variation of lenses capable of various beam steering angle.

Table 7: Lens dimension values for lens capable of various beam steering angle.

Beam Angle	Elliptical Lens		Eccentricity optimized		
	Diameter (mm)	Height (mm)	Diameter (mm)	Height (mm)	eccentricity
0	155	171	155	171	1
1	160	177	160	177	1
2	166	183.19	166	183.19	1
3	176	194.23	176	194.23	1
4	190	209.68	188	209	0.98
5	220	242.7	204	228.35	0.95

5.8 Summary

In this chapter, the relation between the lens parameters and characteristics was established and two lenses were designed to meet given objectives. The lens dimensions are related to permittivity of material used. The directivity of the lens is directly proportional to the lens diameter. The losses of the lens can be minimized by

using material with low loss tangent and dielectric constant between 3 to 5. Higher directivity feed also help reducing spillover loss. Real materials such as Quartz crystal, fused silica, and boron nitride gave better lens characteristics as compared to HDPE but their commercial availability and manufacturing aspect is yet to be analysed. Two lenses were designed to meet given objectives at boresight and upto 5° beam steering angle respectively. Dimension of the lens can be further reduced with higher directivity of the feed array elements, and lens material with dielectric properties in range specified in section 5.4. In order to have a higher directivity feed antenna an increased antenna size is required, but the available inter antenna spacing is limited by -3 dB beam overlapping criteria and dielectric properties of material used in the lens. Therefore, a higher directivity of the feed antenna would increase coupling effect between the switching array elements and a trade-off is required.

6 Dielectric Properties Measurement

6.1 Introduction

Lens characteristics greatly depend on dielectric properties of the material used. Detailed effects of dielectric constant and loss tangent on the lens performance are illustrated in section 5.2. Dielectric properties of material are verified by measurement before the lens fabrication.

When electromagnetic waves travel through any object, a part of the energy is reflected, transmitted, and absorbed. The amount of energy falling into these categories is determined by the dielectric properties of material [83]. Complex dielectric permittivity consists of a real part and an imaginary part:

$$\epsilon = \epsilon^{'} - j \cdot \epsilon^{''}. \tag{42}$$

The real part $\epsilon^{'}$ of complex permittivity is called dielectric constant which expresses materials' capacity to store electric energy and imaginary part $\epsilon^{''}$ is called loss factor that measures energy loss in material due to electric field [75].

Dielectric properties vary with the operating frequency and temperature [75]. Loss tangent and dielectric constant of material is sensitive to the material preparation process. Results of material properties may differ based on the used measurement technique, conditions of measurement and frequency range of measurement [75]. There are various methods for measurement in millimeter and submillimeter band. Transmission/reflection line method, resonant method, free space method, waveguide technique and open-ended coaxial probe method are few of many [84]. In this project, material properties are measured with the free space method.

6.2 Free Space Method

In the free space method, material properties are calculated from the measured value of reflection and transmission coefficient. Material under test (MUT) is placed between spot-focusing transmitting and receiving antennas and transmission and reflection coefficients are measured with a network analyzer in the free space environment. Free space method can be used for measuring both electric and magnetic properties estimation at high frequencies [85]. It does not need special sample preparation.

Total transmission and reflection coefficient measured after multiple reflection inside the material under test are given by [86]:

$$S_{21} = \frac{(1-\Gamma^2)T}{(1-\Gamma^2T^2)}, \qquad S_{11} = \frac{(1-T^2)\Gamma}{(1-\Gamma^2T^2)} \tag{43}$$

where T and Γ are transmission and reflection coefficients respectively. Transmission

and reflection coefficients are given by following equations.

$$T = e^{-\alpha d} \tag{44}$$

$$\Gamma = \frac{Z_{sn} - 1}{Z_{sn} + 1} \tag{45}$$

where α_d is the attenuation coefficient of MUT. Further, loss tangent is calculated from attenuation coefficient α_d using equation (13). Dielectric constant ϵ_r can also be calculated using time difference of arrival method [87]. Permittivity can be estimated by relation

$$\epsilon_r = \left(\frac{C_0 \cdot t_d}{t} \right)^2 \tag{46}$$

where, t_d is time delay travelling through material in comparison to material free space propagation time, t is the thickness of material, and C_o is the free space wave velocity.

The inaccuracies in dielectric measurements using free space method are mainly due to edge diffraction effects and multiple reflections from material-air interface [88]. The diffraction effect can be minimized by satisfying condition $D > 3 \cdot d$ where D and d are minimum material dimension and beam width respectively that leads to large material size. Use of focusing lenses helps minimize the diffraction effect. Reflection effects can be reduced by using thru, reflect and line (TRL) calibration techniques.

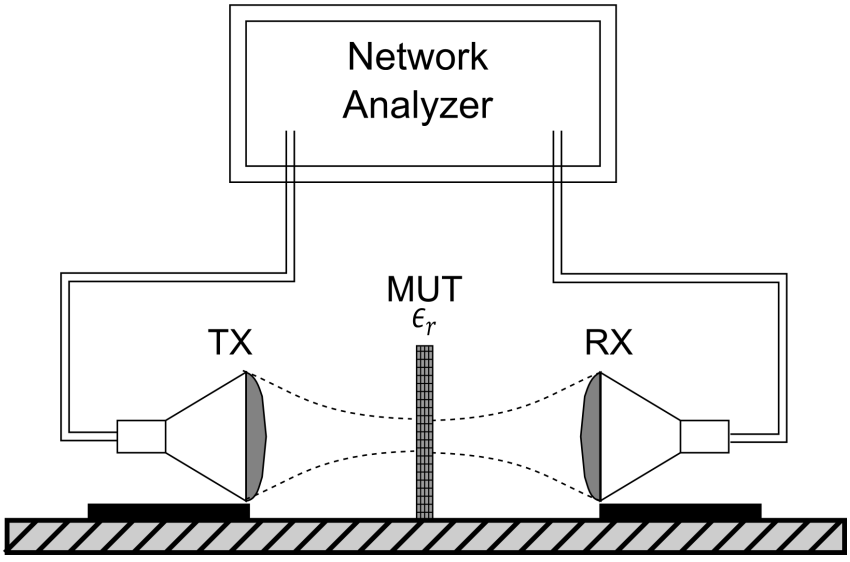

Figure 38: Setup for measuring dielectric properties of sample in free space.

Reflection effects and multi-path interference in free space measurements can be filtered with time gating method (TGM) [86]. TGM transforms frequency domain

measurement data to time domain response with Fourier transform. Then, unwanted reflection response is filtered out based on the time of arrival of the signal. Filtered response is then transformed to the frequency domain. In TGM techniques, minimum time domain gate width is a function of frequency span of the measurement.

6.3 Measurement

Five cylindrical and cubical slabs with varying S1, S2, S3, S4 and S5 with thickness 5 mm, 10 mm, 20 mm, 30 mm, and 50 mm of HDPE and Preperm material respectively were prepared. Free space measurement setup with Keysight N5225 VNA (Vector Network Analyzer) was arranged and V-band transmitter/receiver and receiver extension module were used as shown in Figure 39. Enhanced response calibration is done with open, short, load and thru calibration. Then, Pickett-Potter horn antennas operating at frequency of 50-75 GHz were connected in both TX and RX side as shown in Figure 39. Spot focus lens or parabolic mirrors were not available for the measurement. Absorbers were placed near horn aperture to avoid reflection from unwanted surfaces as shown in Figure 39 (b). Then, total transmission coefficient and reflection coefficient was measured for slabs with varying thickness.

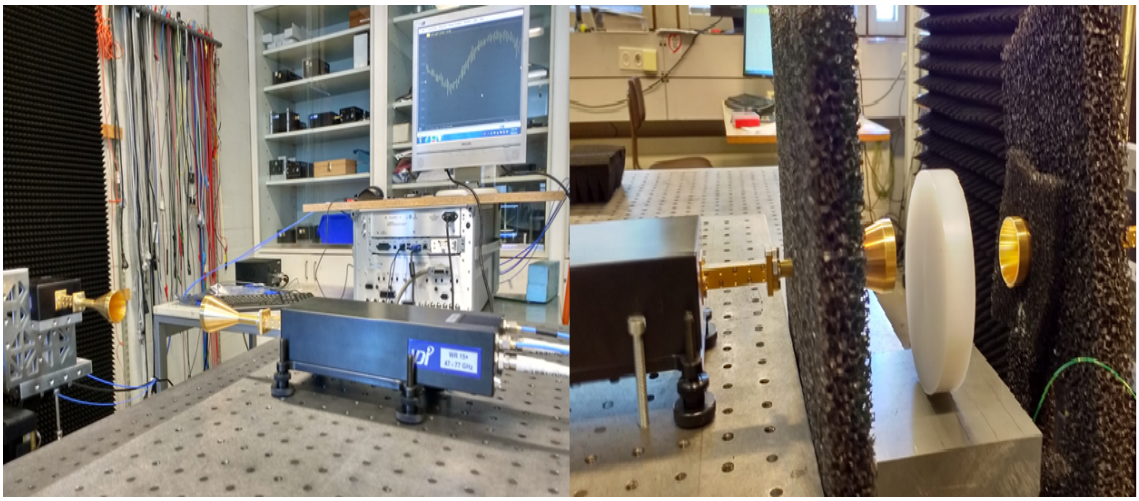

(a) (b)

Figure 39: (a) Free space measurement setup, and (b) measurement setup with absorbers and MUT.

6.4 Result

Measured data was transformed to the time domain in MATLAB using inverse Fourier transform. The resulting time domain data is shown in Figure 40. The difference in the time arrival of signals based on slab thickness is clearly seen in Figure 40. Based on the difference in time of arrival the dielectric constant was calculated using equation (46). In the calculation the arrival time difference between different

thickness of the material was used, i.e. S5-S4, S5-S3, S5-S2, and S5-S1 and difference in thickness of the sample was used in equation 46. Calculation result is presented in Table 8.

Average dielectric permittivity of HDPE is found to be 2.31 for varying slab thickness whereas average dielectric permittivity of Preperm is found to be 5.

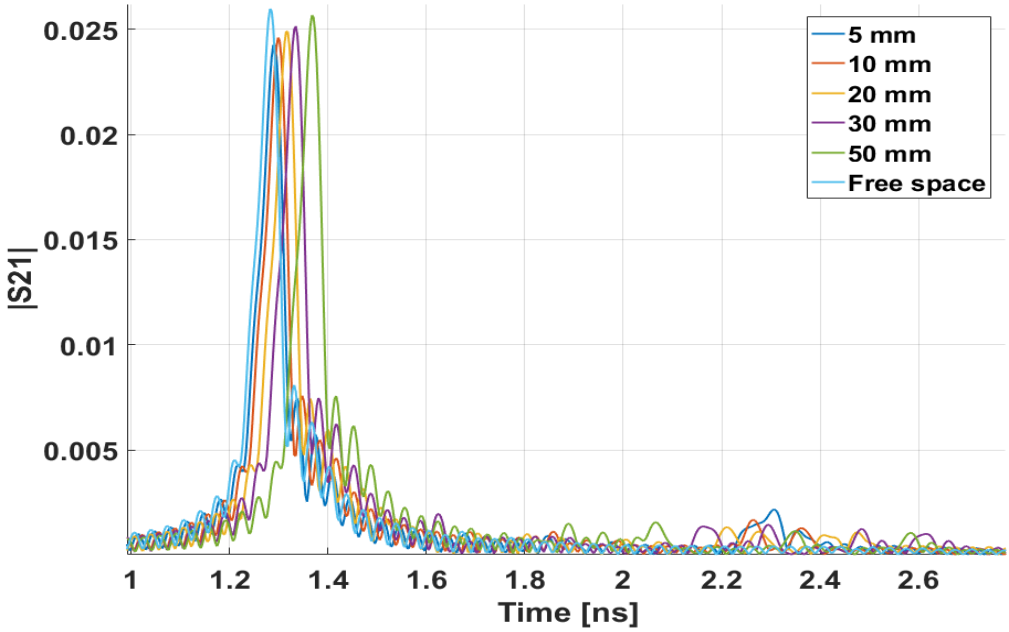

Figure 40: Time domain response of S_{21}.

Table 8: Measured permittivity of HDPE material

Separation (mm)	Horn Distance (mm)	S5-S1	S5-S2	S5-S3	S5-S4
100	40	2.327	2.31	2.31	2.316
	20	2.308	2.304	2.307	2.303
177	40	2.302	2.305	2.30	2.298
	80	2.308	2.307	2.310	2.307
224	40	2.311	2.306	2.310	2.321
	80	2.316	2.314	2.307	2.312

6.5 Loss Tangent Retrieval

After that time gating filter is applied in MATLAB to remove effect of multiple reflections. Gated signal response is shown in Figure 41.

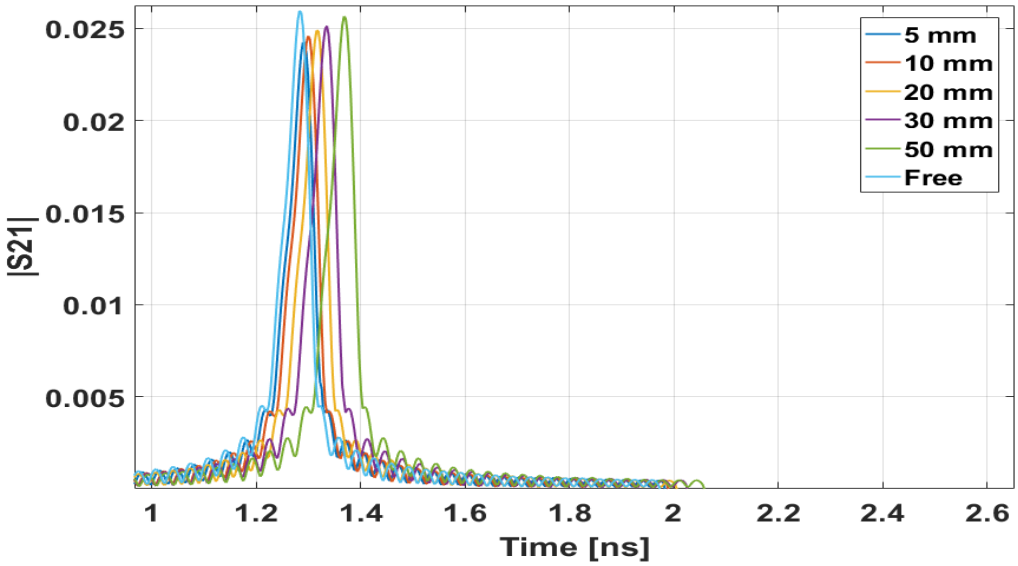

Figure 41: Time gated response of HDPE material at 177 mm horn distance.

Time domain response is transformed to frequency domain using Fourier transform action. Finally, loss tangent is calculated using above equations (43), (45), and (13). Loss tangent graph of HDPE material with respect to frequency is shown in Figure 42 and 43.

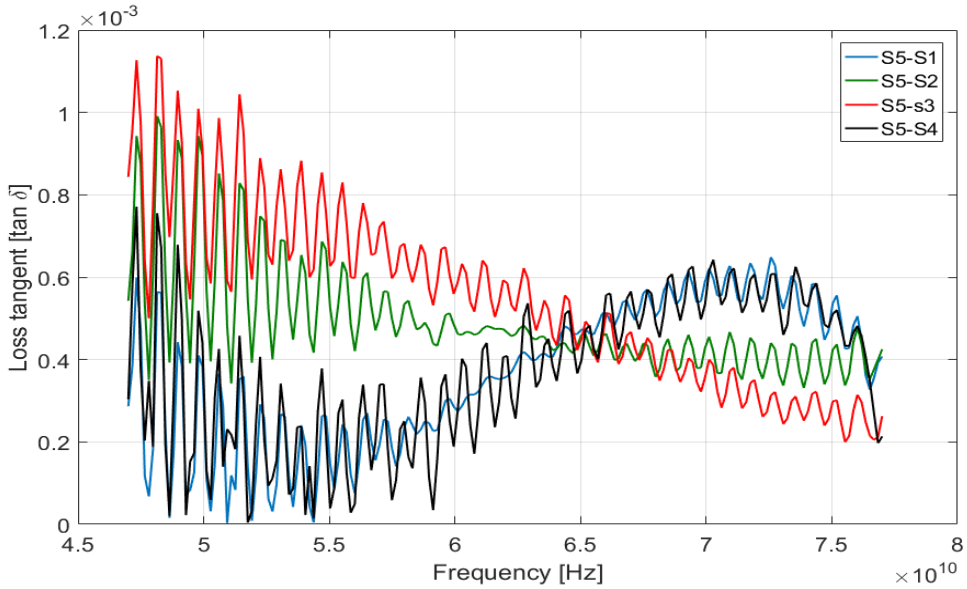

Figure 42: Values of the loss tangent calculated from measured transmission coefficient for HDPE material for varying thickness with 177 mm horn separation distance.

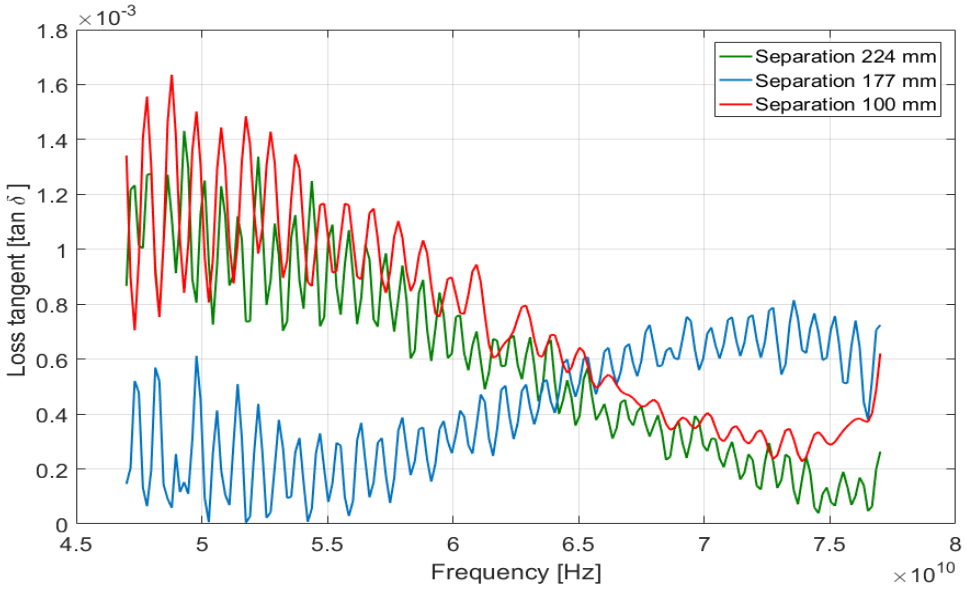

Figure 43: Values of the loss tangent calculated from measured transmission coefficient for different horn separation distance with S5−S4 thickness.

The obtained loss tangent values are in the same range as found from the literature but as the graph shows a lot of variation in the loss tangent depending on the horn separation distance. As focusing lens or mirrors are not used in the measurement setup, there seems to be diffraction effects. Ideally, material under test is assumed to be in far field distance of horn and plane wave is incident on MUT but in this measurement setup MUT is in the near field of horn that affect measurement results. Additionally, free space loss between horn antennas increases discrepancies of result.

6.6 Summary

In this chapter, the theory related to the free space dielectric properties measurement was presented followed by measurements. Free space measurement gave accurate results for dielectric constant ϵ_r. The obtained loss tangent values are in similar range as found in the references but lots of fluctuation were observed. Reason for such discrepancies was accounted for diffraction effects. As radiation pattern of lens depends on dielectric constant, the accurate measurement of dielectric constant of the material at E-band allows precise radiation characteristics prediction with simulation. Though loss tangent could not be retrieved accurately, it only affects lens losses not the radiation pattern or focusing properties. Therefore, we move forward to fabrication and measurement process with the HDPE material.

7 Lens Fabrication and Measurement

7.1 Fabricated Lens

First Lens satisfying the boresight gain criteria is manufactured. The two-dimensional shape of the lens along with its dimensions is shown in Figure 44 (a). The manufactured lens with the absorber and supporting structures is shown in Figure 44 (b).

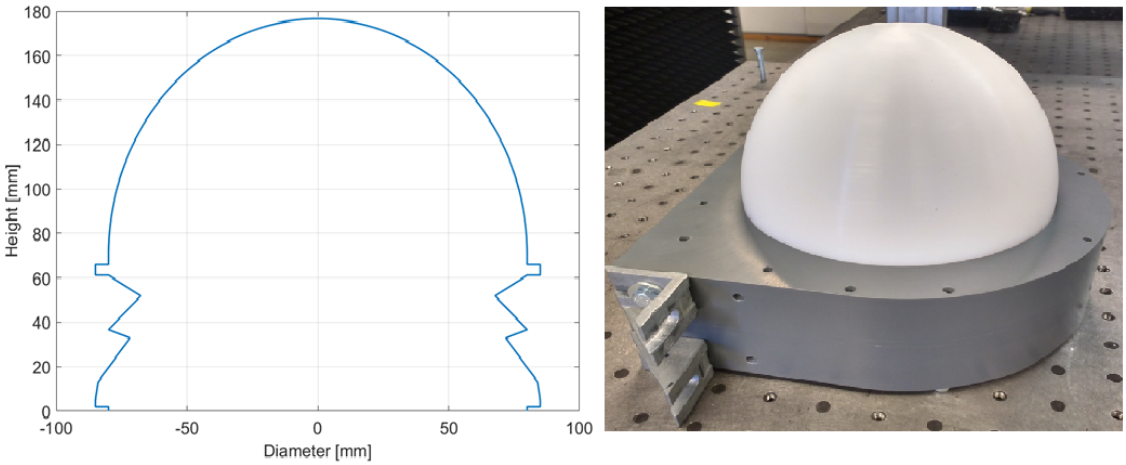

(a) (b)

Figure 44: (a) 2D shape of designed lens and (b) manufactured lens with supporting structures.

7.2 Planar Near-field Measurement

Electromagnetic field of an antenna is mainly divided into three regions: reactive near field region, radiative Near-field region and far-field region. Generally, Far-field radiation pattern of an antenna is generally measured in far-field region where field distribution becomes independent of distance. far-field distance from an antenna is approximated by the relation

$$r = \frac{2 \cdot D^2}{\lambda} \tag{47}$$

where D is maximum antenna dimension and λ is free space wavelength. At higher frequencies, λ becomes smaller and far-field distance increases. Therefore, direct measurement of the far-field radiation pattern is not feasible for electrically large antenna at higher frequencies.

Near-field measurement of an antenna is based on plane-wave spectrum representation of fields [89]. Electric field is measured at near field in a planar surface. Plane wave spectrum is calculated from measured electric field ($\overline{E}_{meas}$) using the

following equation [90]:

$$\overline{A}(kx, ky) = \frac{1}{2\pi} \int_{-\infty}^{\infty} \int_{-\infty}^{\infty} \overline{E}_{meas}(x, y, z) \cdot e^{j\overline{k}\overline{r}} dxdy \tag{48}$$

Then far-field is calculated using plane-wave spectrum vector ($\overline{A}(kx, ky)$) by the following equation:

$$E_{far-field} = \frac{je^{-jkr}}{r} k_z A(kx, ky) \tag{49}$$

Accuracy of the near-field measurement depends on the measurement area, the sample spacing and the separation distance between the AUT aperture and the planar scanning plane. The spatial sampling interval of a half a wavelength is good enough to give accurate results. For electrically large antennas the effect of evanescent modes has virtually no effect so the scanning plane can be at $1 \cdot \lambda$ spacing or even nearer [91].

7.3 Measurement

The far-field radiation pattern of the lens antenna is calculated from planar the measured Near-field data. WR-10 waveguide is used as the feed source. The directivity of waveguide is 8.27 dB which is almost equal to that of ACMA, i.e. 8 dB used for simulations in Chapter 5.

Measurement setup with Keysight N5225 VNA and the lens are shown in Figure 45. V-band extension modules were used in transmitter and receiver ends to transform microwave frequency from VNA to V-band frequencies. Enhanced response calibration is done with short, load and through calibration. In transmitter side, WR-12 to WR-10 transition was used between the extension and WR-10 waveguide to minimizes reflection loss. In receiver side, such a transition was not available so some loss is expected in receiver end.

The receiver is placed on a 2D positioner that is controlled by a Labview program. Distance between the scanning plane and the lens is 37 mm. The scanning plane of 320 mm $\times$ 320 mm in XY plane is assigned. The field outside this scanning plane is considered negligible in this measurement. The sampling interval of 2 mm is assigned based on $\lambda/2$ requirement. Scanner velocity was set to 10 mm/s.

Measurements were taken at four different feed offsrt positions, i.e. 0 mm, 2.3 mm, 9.2 mm, and 18.4 mm. Positioning and aligning of the feeding waveguide is done manually, therefore, some error is expected. Absorbers were placed on both transmitter and receiver end to minimize reflection effects as shown in Figure 46 (b). Near-field measurement of a horn antenna with known gain is done to estimate the gain of the lens antenna and to calibrate the losses in the measurement setup.

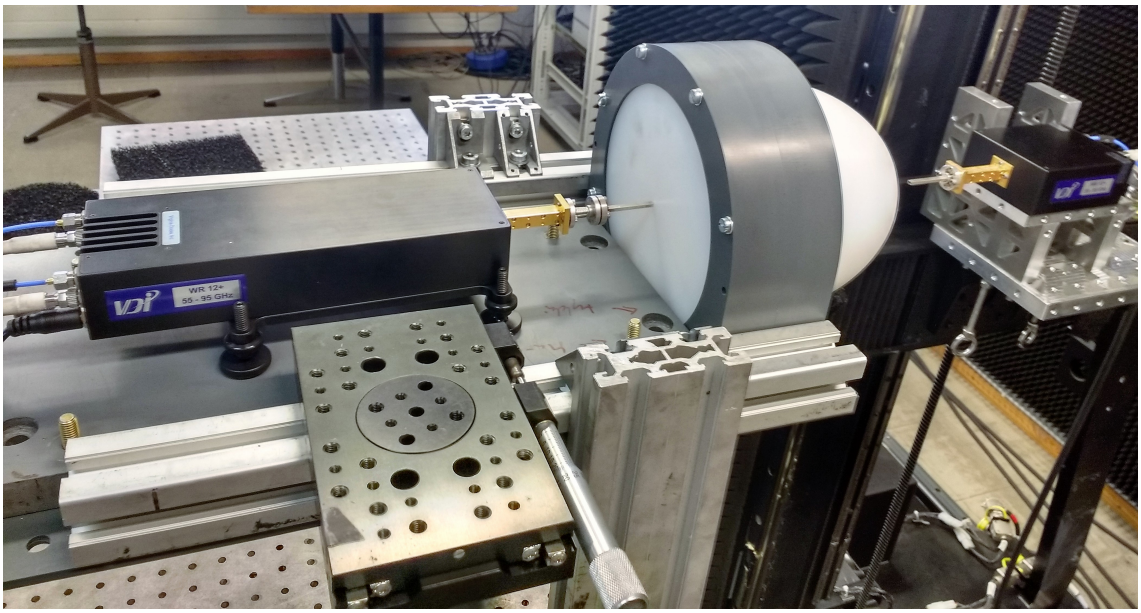

Figure 45: Near-field measurement setup for the lens antenna.

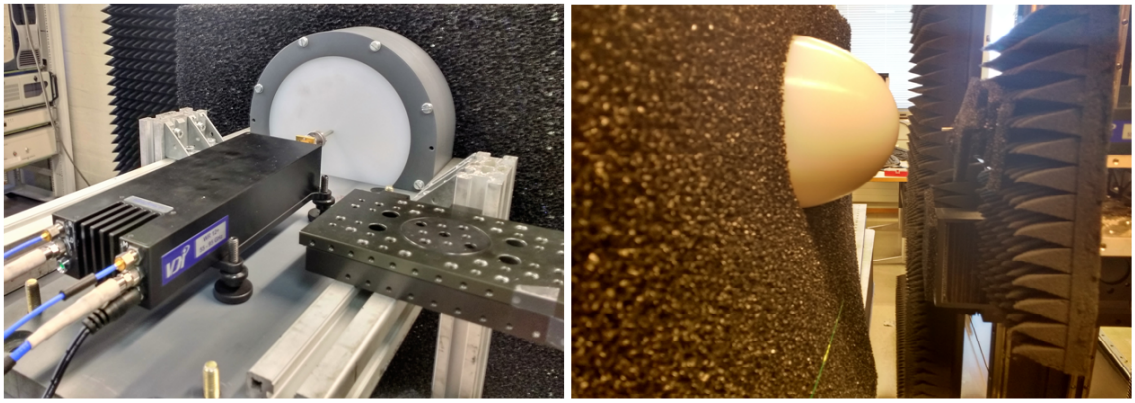

(a) (b)

Figure 46: (a) Feed antenna positioning and (b) absorbers placement in measurement setup.

7.4 Result

Measured Near-field data was transformed to far-field in MATLAB using Fourier transform technique. The reference horn of known 18 dBi gain is used to estimate losses of the measurement setup. Loss of 1.7472 dB in the measurement setup was calculated from the horn antenna measurement. It was compensated in the far-field calculation of the lens. Detail values of simulation and measurement results of the 160 mm HDPE lens with WR-10 waveguide feed are mentioned in Table 9. Results for boresight, 9.2 mm offset and 18.4 mm offset feed is mentioned to evaluate beam-steering properties of the lens at boresight, 5° and 10° beam steering angles respectively.

The comparison between the simulated and measured boresight gain radiation pattern is shown in Figure 47. Gain, HPBW, and side lobe level values from simulation and measurement were almost equal. Figure 47 also shows that boresight radiation pattern meets class 2 RPE regulation. Main beam angle with zero offset feed should point exactly towards boresight as shown in simulation results. But, measured boresight main lobe is tilted -0.85 ° , which suggests that either feed was not placed perfectly at focal center of the lens or the scanner plane and the lens were not aligned precisely. Higher side lobes can be observed in the measured result after ± 50°. At higher beam steering angles side lobes are stronger compared to boresight as shown in Figure 48. Effect of higher order reflected rays within the lens is a most likely reason for such phenomena of sidelobe. Also, limited scanning range limits the accuracy of the result at far angles.

Table 9: Comparison between the measured and simulated results

Feed offset (mm)	Characteristics	Simulated	Measured
0	Gain (dBi)	38.23	38.11
	Beam angle (°)	0.00	-0.85
	Side lobe level (dB)	-16.45	-17.61
	HPBW (°)	1.40	1.48
9.2	Gain (dBi)	36.76	36.07
	Beam-steering angle (°)	5.30	4.85
	Side lobe level (dB)	-10.56	-11.22
	HPBW (°)	1.48	1.51
	Scan loss (dB)	1.52	2.05
18.4	Gain (dBi)	34.21	31.69
	Beam-steering angle (°)	10.31	11.15
	Sidelobe level (dB)	-7.78	-12.69
	HPBW (°)	1.80	2.64
	Scan loss (dB)	4.02	6.41

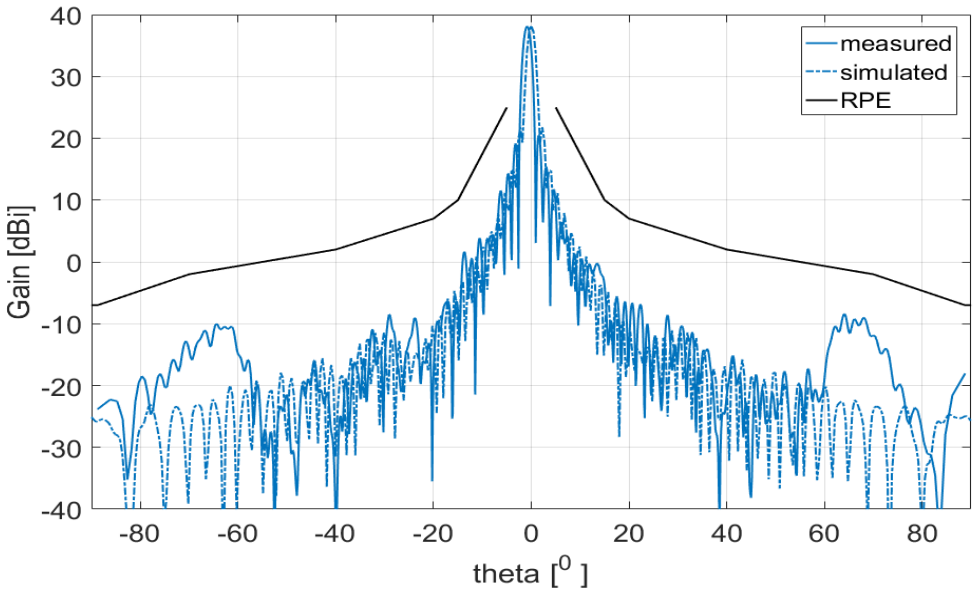

Figure 47: Measured and simulated results of boresight gain pattern.

Scan loss at 5° and 10° beam steering angle were predicted to be 1.52 dB and 4.02 dB respectively with simulation results. Measured results show 2.05 dB and 6.41 dB scan loss at respective beam steering angles as shown in Figure 48 and Figure 49. The probe correction is not applied to the near-field to far-field transformation which partly explains the difference. Further analysis will be carried out later.

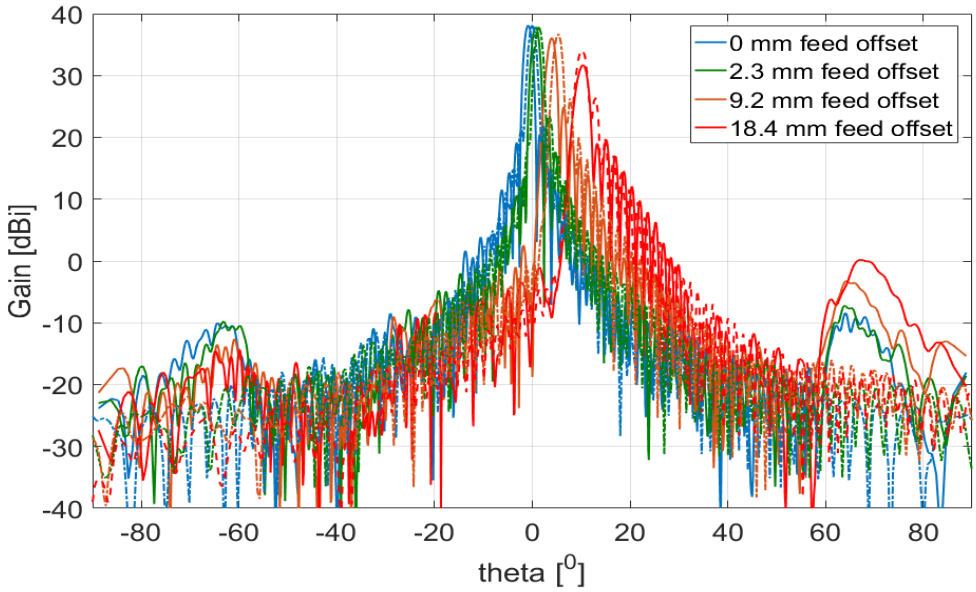

Figure 48: Measured and simulated (dashed) radiation pattern for 0 mm, 2.3 mm, 9.2 mm, and 18.4 mm feed offset position.

The radiation pattern of focal center feed and 2.3 mm feed offset position can be

observed in Figure 49. Simulation results predict 2.3 mm antenna spacing between feed switching array would maintain -3 dB beam overlapping for 160 mm HDPE lens but measurement results show -3.25 dB beam overlap.

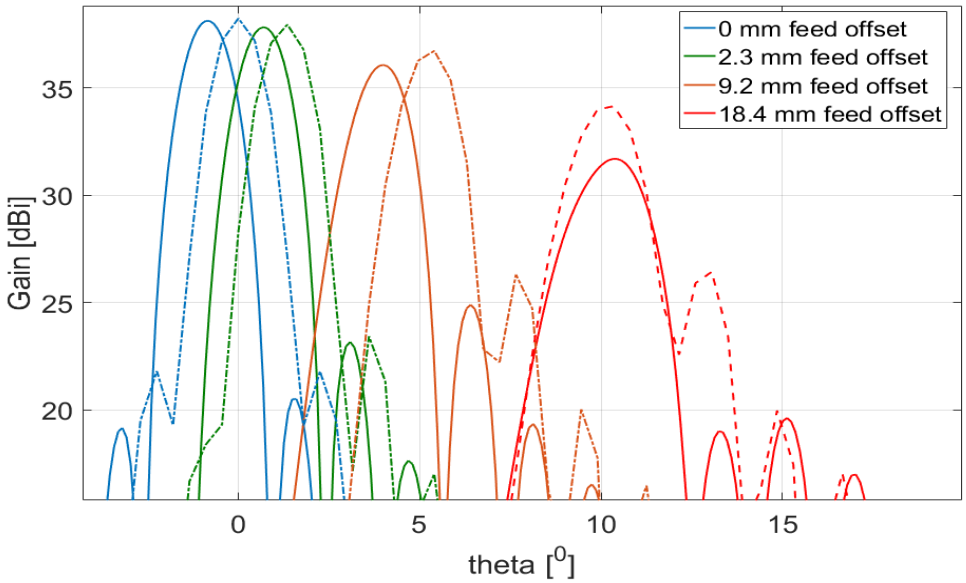

Figure 49: Zoomed measured and simulated (dash) radiation pattern for 0 mm, 2.3 mm, 9.2 mm, and 18.4 mm feed offset position.

7.5 Summary

Mainly, in this chapter measurement and simulation results for First Lens were compared based on gain, beam steering, HPBW and scan loss characteristics. The measured result shows boresight beam has 38.11 dB gain, 1.48° HPBW, -17.61 dB sidelobe level and also meet the class 2 RPE criteria. Small difference between the beam steering angles of measured and simulated results for the same offset feed was observed. Such a difference is mainly caused by inaccuracies in feed positioning and alignment error between the lens and receiver in measurement setup. Stronger side lobes were observed in measurement result at angles more than ± 50 ° . Effect of higher order reflected rays within the lens and limited scan range are most likely reasons for higher sidelobes. Measured results showed high scan loss of 2.05 dB and 6.41 dB for 5° and 10° beam-steering angles respectively, which is higher compared to simulated ones.

8 Conclusions

With demands for high data rate and the exponential increase of connected devices, current network is predicted to have congestion by 2020. High throughput requirement together with complex and dense network structure of 5G demands for flexible and high capacity backhaul link solution. Phased array, reflector antenna, reflectarray, Fresnel zone plate lens and integrated lens antennas were studied briefly and found to be feasible for millimeter wave beam steering application. In this Master's thesis, we considered an elliptical integrated lens antenna (ILA) for wireless backhaul link application.

The main objective of the thesis is to design an ILA with 2D beam steering capability that complies with the point−to−point link antenna regulations for E−band frequency. The ILA performance is mainly evaluated against the 38 dBi gain criteria, class 2 radiation pattern envelope (RPE) criteria, and −25 dB or lower cross−polarization discrimination criteria. The ILA should be capable of ± 5° beam steering and the regulations must be met for each beam steering angle. Lens antenna is electrically large structure, therefore ray tracing simulation is used in this thesis to verify antenna characteristics. Farfield radiation pattern of aperture coupled patch antenna with 8 dB directivity is used as the feed source in ray tracing simulation.

The directivity of the lens is directly proportional to its diameter. Height is proportional to diameter and permittivity of the lens material. Therefore, the lens dimensions depend on dielectric constant of the lens material and directivity requirement. Beam steering angle of the ILA antenna is directly proportional to the feed offset distance and height of the lens. Antenna spacing between switched feed array elements to maintain −3 dB beam overlapping criteria decreases with increasing dielectric constant. For HDPE material ($\epsilon_r = 2.3$) antenna spacing is 2.3 mm whereas for PREPERM ® L450 ($\epsilon_r = 4.5$) material antenna spacing is 1.4 mm.

Losses in the ILA can be categorized into three categories: spillover loss, dielectric loss, and reflection loss. Dielectric loss of ILA is proportional to loss tangent ($\tan\delta$) and dielectric constant ϵ_r. Reflection loss is directly proportional to dielectric constant and feed offset position. Spillover loss is inversely proportional to dielectric constant and feed directivity. Dielectric constant ϵ_r is a common parameter between different type of losses but plays different role in these loss performances and a trade−off analysis is needed for optimum value. Parametric sweep of dielectric constant showed ϵ_r between 3−5 would give minimum loss and maximum gain.

Higher feed directivity helps to reduce spillover loss but after a certain limit amplitude taper reduces lens directivity. Simulation results showed 12 dB feed directivity would be the optimum value till then the effect of the amplitude taper effect in the lens aperture is negligible. Higher feed directivity requires larger aperture area for the feed antenna but − 3 dB beam overlapping criteria limits the feed

antenna spacing. Additionally, decreasing antenna spacing will increase coupling between array element that can degrade radiation properties of the lens. Therefore, maximum achievable feed directivity depends on material permittivity.

Real materials such as Quartz crystal ($\epsilon_r = 4.4$ and $\tan\delta = 0.00051$), fused silica (ϵ_r= 3.81 and $\tan\delta = 0.00055$), and boron nitride ($\epsilon_r = 4.20$ and $\tan\delta = 0.00064$) gave better gain performance compared to HDPE but their commercial availability and manufacturing aspect is yet to be analyzed. PREPERM ® L450 material with dielectric constant ϵ_r 5 (measured in this project) and loss tangent $\tan\delta$ 0.0046 (from reference) from Premix Oy have dielectric constant ϵ_r in the range with our optimization results but loss tangent $\tan\delta$ of material was too high to be used in lens design. HDPE material was the best commercially available option due to low loss tangent ($\tan\delta = 0.0003$) value.

Two lenses were designed with HDPE material to meet given objectives at boresight and up to 5° beam steering angle respectively. First Lens of 160 mm diameter and 177 mm height was designed to meet 38 dBi gain criteria only at boresight. Second Lens with 210 mm diameter and 236 mm height was designed to meet the gain criteria up to 5° beam steering angle. The eccentricity of Second Lens was optimized to 0.95 in order to minimize scan loss. Both lenses meet class 2 radiation pattern envelope criteria up to designed beam steering range. Cross polarization level for both lenses were simulated to be below -26 dB for all beam steering range.

In order to verify simulation results First Lens was fabricated for measurement. Extension section of First Lens was redesigned with grooved structure to minimize reflections so that radiation from the extension does not impact farfield radiation pattern. Increasing dimensions of the lens helps to meet the gain criteria at higher beam steering angle but from the manufacturing and application perspective, bigger lenses are challenging. Therefore, the trade-off analysis is done between the lens dimension and beam steering angle to find suitable value for application purpose.

As lens characteristics are critically dependent on the dielectric properties of the material used, especially dielectric constant ϵ_r. Free space dielectric properties measurement method was used to measure dielectric constant and loss tangent of available HDPE material before the lens fabrication. Dielectric constant ϵ_r of HDPE was found to be 2.31. The obtained loss tangent $\tan\delta$ value showed fluctuation between $(0.2-0.8)\times10^{-3}$. Reason for such discrepancies was accounted for diffraction effects.

First Lens measurement result showed boresight beam has 38.11 dB gain, 1.48° HPBW, and -17.61 dB side lobe level. Boresight radiation pattern meets class 2 RPE criteria. Small differences between the measured and simulated beam steering angles for the same offset feed position was observed. Such difference is mainly caused by inaccuracies in feed positioning and alignment error between the lens and the receiver in measurement setup. Stronger side lobes were observed in measurement

result at angles more than $\pm$ 50°. Effect of higher order reflected rays within lens may be a reason for higher side lobes. Near−field measurement is time consuming measurement process. Limiting scan range reduces measurement time but accuracy at far angles is also limited. Measured results showed scan loss of 2.05 dB and 6.41 dB for 5° and 10° beam-steering angles respectively. Measured scan loss are higher compared to simulation results.

Next step in ILA development process would be measuring the lens performance with ACMA feed array. Also, the lens performance in entire E-band (71−76) GHz/ (81−86) GHz spectrum should be studied. Understanding effects of higher order reflection in the lens is important to precisely predict radiation pattern. Further efforts should be made in finding materials having dielectric properties as recommended in section 5.4. Implementation of performance optimization methods studied in section 3.5 should also be considered in design and manufacturing process. Feed array coupling effect for different permittivity lens material should be studied.

References

[1] J. G. Andrews, S. Buzzi, W. Choi, S. V. Hanly, A. Lozano, A. C. Soong, and J. C. Zhang, "What will 5 g be?" *IEEE Journal on Selected Areas in Communications*, vol. 32, no. 6, pp. 1065–1082, 2014.

[2] N. Solutions and Networks, "Looking ahead to 5G," White Paper, April 2016.

[3] Ericsson, "5G radio-access," White Paper, April 2016.

[4] N. Bhushan, J. Li, D. Malladi, R. Gilmore, D. Brenner, A. Damnjanovic, R. T. Sukhavasi, C. Patel, and S. Geirhofer, "Network densification: the dominant theme for wireless evolution into 5G," *IEEE Communications Magazine*, vol. 52, no. 2, pp. 82–89, 2014.

[5] J. Thompson, X. Ge, H.-C. Wu, R. Irmer, H. Jiang, G. Fettweis, and S. Alamouti, "5G wireless communication systems: prospects and challenges [guest editorial]," *IEEE Communications Magazine*, vol. 52, no. 2, pp. 62–64, 2014.

[6] R. J. Weiler, M. Peter, W. Keusgen, E. C. Strinati, A. De Domenico, I. Filippini, A. Capone, I. Siaud, A.-M. Ulmer-Moll, A. Maltsev *et al.*, "Enabling 5G backhaul and access with millimeter-waves," in *2014 European Conference on Networks and Communications EuCNC*, Bologna, Italy, June 2014, pp. 1–5.

[7] R. Taori and A. Sridharan, "Point-to-multipoint in-band mmwave backhaul for 5G networks," *IEEE Communications Magazine*, vol. 53, no. 1, pp. 195–201, 2015.

[8] D. A. Bell, *Information theory and its engineering applications*. Pitman Publishing, 1968.

[9] W. Feng, Y. Li, D. Jin, L. Su, and S. Chen, "Millimetre-wave backhaul for 5G networks: Challenges and solutions," *Sensors*, vol. 16, no. 6, p. 892, 2016.

[10] C. Dehos, J. L. González, A. De Domenico, D. Kténas, and L. Dussopt, "Millimeter-wave access and backhauling: the solution to the exponential data traffic increase in 5G mobile communications systems?" *IEEE Communications Magazine*, vol. 52, no. 9, pp. 88–95, 2014.

[11] B. Ayvazian and C. Hetting, "Second-generation E-band solutions: Opportunities for carrier-class LTE backhaul," *Heavy Reading white paper (February 2013)*, 2013.

[12] T. S. Rappaport, S. Sun, R. Mayzus, H. Zhao, Y. Azar, K. Wang, G. N. Wong, J. K. Schulz, M. Samimi, and F. Gutierrez, "Millimeter wave mobile communications for 5G cellular: It will work!" *IEEE access*, vol. 1, pp. 335–349, 2013.

[13] P. Adhikari, "Understanding millimeter wave wireless communication," *Loea Corporation*, 2008.

[14] S. Hur, T. Kim, D. J. Love, J. V. Krogmeier, T. A. Thomas, and A. Ghosh, "Millimeter wave beamforming for wireless backhaul and access in small cell networks," *IEEE Transactions on Communications*, vol. 61, no. 10, pp. 4391–4403, 2013.

[15] ETSI, "Fixed Radio System; Characteristics and requirement for point-to-point equipment and antennas ," European Telecommunications Standards Institute, Tech. Rep., 2008.

[16] T. Veijalainen, "Beam steering in millimeter wave radio links for small cell mobile backhaul," *M. Sc.(Tech.) thesis, Aalto University*, 2014.

[17] Commscope, "Reducing the risk to backhaul links in the integrated radio-to-antenna path," White Paper, February 2016.

[18] A. Karttunen, "Millimetre and submillimetre wave antenna design using ray tracing," *PhD dissertation, Aalto University*, 2013.

[19] I. Uchendu and J. R. Kelly, "Survey of beam steering techniques available for millimeter wave applications," *Progress In Electromagnetics Research B*, vol. 68, pp. 35–54, 2016.

[20] T. A. Milligan, *Modern antenna design.* John Wiley & Sons, 2005.

[21] W. Hong, K.-H. Baek, Y. Lee, Y. Kim, and S.-T. Ko, "Study and prototyping of practically large-scale mmwave antenna systems for 5G cellular devices," *IEEE Communications Magazine*, vol. 52, no. 9, pp. 63–69, 2014.

[22] S. K. Garakoui, E. A. Klumperink, B. Nauta, and F. E. van Vliet, "Phased-array antenna beam squinting related to frequency dependency of delay circuits," in *41st European Microwave Conference (EuMC), 2011.* Manchester, UK: IEEE, October 2011, pp. 1304–1307.

[23] O. Bakr and M. Johnson, "Impact of phase and amplitude errors on array performance," *EECS Department, University of California, Berkeley, Tech. Rep. UCB/EECS-2009-1*, 2009.

[24] T. Leinonen, "Aligning and tracking a beam steerable millimeter-wave radio link," 2015.

[25] W. L. Stutzman and G. A. Thiele, *Antenna theory and design.* John Wiley & Sons, 2012.

[26] J. D. Kraus, *Antennas.* McGraw−Hill Education, 1988.

[27] A. W. Rudge and N. A. Adatia, "Offset-parabolic-reflector antennas: A review," *Proceedings of the IEEE*, vol. 66, no. 12, pp. 1592–1618, 1978.

[28] W. Imbriale, P. Ingerson, and W. Wong, "Large lateral feed displacements in a parabolic reflector," *IEEE Transactions on Antennas and Propagation*, vol. 22, no. 6, pp. 742–745, 1974.

[29] A. V. Mrstik, "Scan limits of off-axis fed parabolic reflectors," *IEEE Transactions on Antennas and Propagation*, vol. 27, no. 5, pp. 647–651, 1979.

[30] R. Assaly and L. Ricardi, "A theoretical study of a multi-element scanning feed system for a parabolic cylinder," *IEEE Transactions on Antennas and Propagation*, vol. 14, no. 5, pp. 601–605, 1966.

[31] J. P. Gianvittorio and Y. Rahmat-Samii, "Reconfigurable patch antennas for steerable reflectarray applications," *IEEE Transactions on Antennas and Propagation*, vol. 54, no. 5, pp. 1388–1392, 2006.

[32] E. Carrasco, M. Barba, M. Arrebola, and J. A. Encinar, "Recent developments of reflectarray antennas for reconfigurable beams using surface-mounted rf-mems," *International Journal of Antennas and Propagation*, vol. 2012, 2012.

[33] J. A. Encinar, "Recent advances in reflectarray antennas," in *Proceedings of the Fourth European Conference on Antennas and Propagation.* Barcelona, Spain: IEEE, April 2010, pp. 1–6.

[34] D. M. Pozar, S. D. Targonski, and H. Syrigos, "Design of millimeter wave microstrip reflectarrays," *IEEE Transactions on Antennas and Propagation*, vol. 45, no. 2, pp. 287–296, 1997.

[35] J. Huang, "Bandwidth study of microstrip reflectarray and a novel phased reflectarray concept," in *Antennas and Propagation Society International Symposium, 1995. AP-S. Digest*, vol. 1. California, USA: IEEE, June 1995, pp. 582–585.

[36] Q. Luo, S. Gao, C. Zhang, D. Zhou, T. Chaloun, W. Menzel, V. Ziegler, and M. Sobhy, "Design and analysis of a reflectarray using slot antenna elements for Ka-band SatCom," *IEEE Transactions on Antennas and Propagation*, vol. 63, no. 4, pp. 1365–1374, 2015.

[37] A. Tamminen, J. Ala-Laurinaho, S. Mäkelä, A. Räisänen, D. G. Martins, J. Häkli, P. Koivisto, P. Rantakari, J. Säily, R. Tuovinen *et al.*, "Millimeter-wave reflectarray for beam-steering applications," in *7th European Microwave Integrated Circuits Conference (EuMIC), 2012.* Amsterdam, Netherland: IEEE, Oct - Nov 2012, pp. 219–222.

[38] J. Thornton and K.-C. Huang, *Modern lens antennas for communications engineering.* John Wiley & Sons, 2013, vol. 39.

[39] C. A. Fernandes, E. B. Lima, and J. R. Costa, "Dielectric lens antennas," *Handbook of Antenna Technologies*, 2015.

[40] H. D. Hristov and M. H. Herben, "Millimeter-wave Fresnel-zone plate lens and antenna," *IEEE Transactions on Microwave Theory and Techniques*, vol. 43, no. 12, pp. 2779–2785, 1995.

[41] H. D. Hristov, *Fresnel Zones in Wireless Links, Zone Plate Lenses and Antennas*. Artech House, Inc., 2000.

[42] I. V. Minin and O. V. Minin, *Basic principles of Fresnel antenna arrays*. Springer Science & Business Media, 2008, vol. 19.

[43] D. N. Black and J. C. Wiltse, "Millimeter-wave characteristics of phase-correcting Fresnel zone plates," *IEEE Transactions on Microwave Theory and Techniques*, vol. 35, no. 12, pp. 1122–1129, 1987.

[44] A. Petosa, N. Gagnon, and A. Ittipiboon, "Effects of Fresnel lens thickness on aperture efficiency," in *Proc. 10th Int. Symp. Antenna Techniques and applications EM and URSI Conf*, Ottawa, Canada, July 2004, pp. 175–178.

[45] A. Petosa and A. Ittipiboon, "Shadow blockage effects on the aperture efficiency of dielectric Fresnel lenses," *IEE Proceedings-Microwaves, Antennas and Propagation*, vol. 147, no. 6, pp. 451–454, 2000.

[46] T. F. Gallacher, D. A. Robertson, and G. M. Smith, "The photo-injected Fresnel zone plate antenna: Optoelectronic beam steering at mm-wave frequencies," *IEEE Transactions on Antennas and Propagation*, vol. 61, no. 4, pp. 1688–1696, 2013.

[47] A. Petosa, S. Thirakoune, and A. Ittipiboon, "Reconfigurable Fresnel-zone-plate-shutter antenna with beam-steering capability," *IEEE Antennas and Propagation Magazine*, vol. 49, no. 5, pp. 42–51, 2007.

[48] G. León Fernández, L. F. Herrán Ontañón, M. Munoz, F. L. Las Heras Andrés, and Y. Hao, "Millimeter-wave offset Fresnel zone plate lenses characterization," *Progress In Electromagnetics Research C, 54*, 2014.

[49] A. Jouad, J. Bor, O. Lafond, and M. Himdi, "Millimeter-wave Fresnel zone plate lens based on foam gradient index technological process," in *2016 10th European Conference on Antennas and Propagation (EuCAP)*. Davos, Switzerland: IEEE, April 2016, pp. 1–4.

[50] A. Artemenko, A. Mozharovskiy, A. Sevastyanov, V. Ssorin, and R. Maslennikov, "Electronically beam steerable lens antenna for 71–76/81–86 ghz backhaul applications," in *2015 IEEE MTT-S International Microwave Symposium*. Phoenix, USA: IEEE, May 2015, pp. 1–4.

[51] J. Ala-Laurinaho, A. Karttunen, and A. V. Räisänen, "A mm-wave integrated lens antenna for E-band beam steering," in *9th European Conference on Antennas and Propagation (EuCAP2015)*. Lisbon, Portugal: IEEE, April 2015, pp. 1–2.

[52] D. F. Filipovic, G. P. Gauthier, S. Raman, and G. M. Rebeiz, "Off-axis properties of silicon and quartz dielectric lens antennas," *IEEE Transactions on Antennas and Propagation*, vol. 45, no. 5, pp. 760–766, 1997.

[53] A. Karttunen, J. Ala-Laurinaho, R. Sauleau, and A. V. Raisanen, "Reduction of internal reflections in integrated lens antennas for beam-steering," *Progress In Electromagnetics Research*, vol. 134, pp. 63–78, 2013.

[54] J. R. Costa, E. B. Lima, and C. A. Fernandes, "Compact beam-steerable lens antenna for 60-GHz wireless communications," *IEEE Transactions on Antennas and Propagation*, vol. 57, no. 10, pp. 2926–2933, 2009.

[55] M. Van der Vorst, P. De Maagt, and M. Herben, "Scan-optimized integrated lens antennas," in *Microwave Conference, 1997. 27th European*, vol. 1. Jerusalem, Isarel: IEEE, September 1997, pp. 605–610.

[56] J. Ala-Laurinaho, A. Karttunen, J. Säily, A. Lamminen, R. Sauleau, and A. V. Räisänen, "Mm-wave lens antenna with an integrated ltcc feed array for beam steering," in *Proceedings of the Fourth European Conference on Antennas and Propagation*. Barcelona, Spain: IEEE, April 2010, pp. 1–5.

[57] T. Nguyen, A. Boriskin, L. Le Coq, and R. Sauleau, "Improvement of the scanning performance of the extended hemispherical integrated lens antenna using a double lens focusing system," *IEEE Transactions on Antennas and Propagation*, vol. 64, no. 1, pp. 3698–3702, August 2016.

[58] X. Wu, G. V. Eleftheriades, and T. E. van Deventer-Perkins, "Design and characterization of single-and multiple-beam mm-wave circularly polarized substrate lens antennas for wireless communications," *IEEE Transactions on Microwave Theory and Techniques*, vol. 49, no. 3, pp. 431–441, 2001.

[59] J. Whitehead and W. Rueggeberg, "The measurement of dielectric loss at high frequencies an under changing temperature," *Transactions of the American Institute of Electrical Engineers*, vol. 68, no. 1, pp. 520–524, 1949.

[60] W. Rotman, "EHF dielectric lens antenna for satellite communication systems," Defense Technical Information Center (DTIC) Document, Tech. Rep., 1983.

[61] T. C. Cheston and J. Frank, "Array antennas," Defense Technical Information Center (DTIC) Document, Tech. Rep., 1968.

[62] A. Karttunen, J. Ala-Laurinaho, R. Sauleau, and A. V. Räisänen, "Optimal eccentricity of a low permittivity integrated lens for a high-gain beam-steering antenna," in *Proceedings of the 5th European Conference on Antennas and Propagation (EUCAP)*. Rome, Italy: IEEE, April 2011, pp. 3522–3526.

[63] F. Tokan, "Optimization-based matching layer design for broadband dielectric lens antennas," *Applied Computational Electromagnetics Society Journal*, vol. 29, no. 6, 2014.

[64] J. R. Costa, M. G. Silveirinha, and C. A. Fernandes, "Evaluation of a double-shell integrated scanning lens antenna," *IEEE Antennas and Wireless Propagation Letters*, vol. 7, pp. 781–784, 2008.

[65] J. Costa, M. Silveirinha, and C. Fernandes, "Design and analysis of double-shell axial-symmetric integrated lens antennas for space applications," in *Proc. 28th ESA Antenna Workshop on Space Antenna Systems and Technologies*, Noordwijk, The Netherlands, May - June 2005, pp. 865–872.

[66] W. Rotman, "Analysis of an EHF aplanatic zoned dielectric lens antenna," *IEEE transactions on antennas and propagation*, vol. 32, no. 6, pp. 611–617, 1984.

[67] Y. Yi and W. Dou, "Analysis and design of dielectric zoned hollow lens antenna at w-band," in *9th International Symposium on Antennas Propagation and EM Theory (ISAPE), 2010*, Guangzhou, China.

[68] A. V. Boriskin, R. Sauleau, and A. I. Nosich, "Performance of hemielliptic dielectric lens antennas with optimal edge illumination," *IEEE Transactions on Antennas and Propagation*, vol. 57, no. 7, pp. 2193–2198, 2009.

[69] D. M. Pozar, "A review of aperture coupled microstrip antennas: History, operation, development, and application," University of Massachusetts at Amherst, Tech. Rep., May 1996. [Online]. Available: http://www.ecs.umass.edu/ece/pozar/aperture.pdf.

[70] A. Mozharovskiy, A. Artemenko, A. Sevastyanov, V. Ssorin, and R. Maslennikov, "Beam-steerable integrated lens antenna with waveguide feeding system for 71-76/81-86 GHz point-to-point applications," in *2016 10th European Conference on Antennas and Propagation (EuCAP)*. Davos, Switzerland: IEEE, 2016, pp. 1–5.

[71] G. A. Deschamps, "Ray techniques in electromagnetics," *Proceedings of the IEEE*, vol. 60, no. 9, pp. 1022–1035, 1972.

[72] T. Komljenovic, Z. Sipus *et al.*, "Raytracing analysis of lens antennas-practical approach," in *ELMAR, 2009. ELMAR'09. International Symposium*, Zadar, Croatia, September, pp. 313–316.

[73] A. S. Glassner, *An introduction to ray tracing*. Elsevier, 1989.

[74] G. E. Athanasiadou and A. R. Nix, "A novel 3-d indoor ray-tracing propagation model: The path generator and evaluation of narrow-band and wide-band predictions," *IEEE transactions on Vehicular Technology*, vol. 49, no. 4, pp. 1152–1168, 2000.

[75] J. W. Lamb, "Miscellaneous data on materials for millimetre and submillimetre optics," *International Journal of Infrared and Millimeter Waves*, vol. 17, no. 12, pp. 1997–2034, 1996.

[76] A. Ludwig, "The definition of cross polarization," *IEEE Transactions on Antennas and Propagation*, vol. 21, no. 1, pp. 116–119, 1973.

[77] V. Parshin, "Dielectric materials for gyrotron output windows," *International journal of infrared and millimeter waves*, vol. 15, no. 2, pp. 339–348, 1994.

[78] J. Dutta, C. Jones, and H. Dave, "Complex dielectric constants for selected near-millimeter-wave materials at 245 GHz," North Carolina Central Univ., Durham (USA), Tech. Rep., 1986.

[79] P. Whibberley and J. Birch, "The temperature variation of the near-mm wavelength optical constants of fluorosint," *Infrared Physics*, vol. 29, no. 6, pp. 995–996, 1989.

[80] M. N. Afsar, "Precision millimeter-wave measurements of complex refractive index, complex dielectric permittivity, and loss tangent of common polymers," *IEEE Transactions on Instrumentation and Measurement*, vol. 1001, no. 2, pp. 530–536, 1987.

[81] M. N. Afsar and K. J. Button, "Millimeter-wave dielectric measurement of materials," *Proceedings of the IEEE*, vol. 73, no. 1, pp. 131–153, 1985.

[82] Premix Oy, "Private communications."

[83] M. Venkatesh and G. Raghavan, "An overview of dielectric properties measuring techniques," *Canadian Biosystems Engineering*, vol. 47, no. 7, pp. 15–30, 2005.

[84] O. Büyüköztürk, T.-Y. Yu, and J. A. Ortega, "A methodology for determining complex permittivity of construction materials based on transmission-only coherent, wide-bandwidth free-space measurements," *Cement and Concrete Composites*, vol. 28, no. 4, pp. 349–359, 2006.

[85] D. K. Ghodgaonkar, V. V. Varadan, and V. K. Varadan, "A free-space method for measurement of dielectric constants and loss tangents at microwave frequencies," *IEEE Transactions on Instrumentation and measurement*, vol. 38, no. 3, pp. 789–793, 1989.

[86] A. Khosrowbeygi, H. Griffiths, and A. Cullen, "A new free-wave dielectric and magnetic properties measurement system at millimetre wavelengths," in *Microwave Symposium Digest, 1994., IEEE MTT-S International*, San deigo, California.

[87] B. Will and I. Rolfes, "Comparative study of moisture measurements by time domain transmissometry," in *Sensor's, 2013 IEEE*. Baltimore, Maryland, USA: IEEE, November 2013, pp. 1–4.

[88] D. Ghodgaonkar, V. Varadan, and V. Varadan, "Free-space measurement of complex permittivity and complex permeability of magnetic materials at microwave frequencies," *IEEE Transactions on instrumentation and measurement*, vol. 39, no. 2, pp. 387–394, 1990.

[89] A. Yaghjian, "An overview of near-field antenna measurements," *IEEE Transactions on Antennas and Propagation*, vol. 34, no. 1, pp. 30–45, 1986.

[90] J. R. Pérez and J. Basterrechea, "A theoretical comparison between three planar near to far-field transformation methods for antenna measurements," *Proceedings of the XXVII General Assembly of the URSI*, 2002.

[91] J. J. Wang, "An examination of the theory and practices of planar near-field measurement," *IEEE Transactions on antennas and propagation*, vol. 36, no. 6, pp. 746–753, 1988.